General comments:

● *The authors have properly addressed previous reviewers' comments. I only have a few minor comments and suggestions.*

We thank the reviewer for the constructive comments. They are very helpful for improving the quality of the manuscript. In the revised manuscript, we add more clarification in the text as the reviewer suggested.

Specific comments:

● *1. Lines 64-67: "This study implies that global climate models generally with even coarser resolutions than 20 km and therefore relatively smoother topography may introduce significant negative biases in estimating light-absorbing aerosol radiative forcing over the TP." I would hesitate to agree with this argument, since there may not be negative biases for global models even with coarser resolution considering different model physics/parameterizations used in global models. The negative bias caused by the topography issue may be canceled out by biases caused by other model processes. If the authors really want to make this argument, they need to be more specific and accurate in stating this to avoid any confusion.*

Thank you for your suggestion. We totally agree with you. In the revised manuscript, we make the statement more specifically as "This study implies that the smoother topography used by global climate models generally with even coarser resolutions than 20 km may introduce significant negative biases in estimating light absorbing aerosol radiative forcing over the TP during the pre-monsoon season." In the Conclusion section, we also clarify it as "Therefore, the relatively smooth topography used by climate models at coarser horizontal resolutions than 20 km may result in the underestimation of aerosol transport from South Asia to the TP during the pre-monsoon season and lead to the biases in distributions of aerosol radiative forcing in the atmosphere and surface snow over the TP."

● *2. One important aspect of the model description that is missing is related to the convective parameterization. Normally, one important advantage for using very high resolution (e.g., < ~4 km) is that WRF-Chem can be run at such resolution without using convective parameterization (commonly known as convection-permitting simulations) to explicitly resolve deep convection. How did the author set up their model simulations regarding this? How is this process coupled with aerosol wet deposition in the model? This is expected to significantly affect aerosol wet scavenging potentially.*

Thanks to raise this. Yes, it is one critical advantage to run high resolution at 4 km or less to avoid using cumulus parameterization. We only used cumulus parameterization for the outer domain at 20 km resolution and it was turned off for the inner domain at

4 km resolution. Now it is clarified in the revised manuscript as "It is noteworthy that the cumulus scheme is only used in the outer domain at 20 km resolution and is turned off in the inner domain at 4 km resolution."

In terms of wet deposition without cumulus parameterization, it was described in the text as "The wet removal of grid-resolved stratiform clouds/precipitation includes two aspects, namely in-cloud removal (rainout) and below-cloud removal (washout) by Easter et al. (2004) and Chapman et al. (2009), respectively."

As our response to the other comment below, although the wet deposition is included in our simulation, we didn't emphasize this process because its impact is quite small during our simulation period. One reason of relatively small impact of wet deposition may be because of inactive convection during the pre-monsoon season. We have discussed in the manuscript that the aerosol-climate interaction with the consideration of complex topography during the monsoon season deserves further investigation.

- *3. The authors used WRF-Chem coupled with the SNICAR model to quantify the radiative forcing of absorbing aerosols in snow. Did the authors assume spherical snow grains externally mixed with aerosols in the model? A recent study (He et al., 2018, https://doi.org/10.5194/acp-18-11507-2018) has updated the SNICAR model to include the treatment of nonspherical snow grains and BC-snow internal mixing, which showed significant impacts on aerosol radiative effect in snow over the TP. Did the authors use this updated SNICAR model? I suggest including some clarifications and discussions on this aspect.*

Thank the reviewer to notice us about this update. We don't include this update in this study. As the reviewer said, this is one of the model uncertainties in other processes, which we believe will not affect our conclusions. We add this clarification in the revised manuscript as "Please note that the SNICAR model was recently updated by He et al. (2018) to include the impact of non-spherical snow grains on aerosol snow-albedo effect that is not included in this study."

- *4. The model spin-up time is only 2 days, which seems not enough to me even for aerosols like BC with a typical lifetime of about one week. Any justification?*

In fact, we have 3-day (March 29-31) for spin up. In general, we have 3-7 days for spin-up of regional modeling of aerosols. 3-day is the lower limit. We chose this in this study to save the computational cost. However, we obtained the initial condition from the quasi-global WRF-Chem simulation during the same period, which will reduce the impacts of initial condition on our results. In addition, from Fig. 8 and Fig. 14, we can see that the pollution transport episode started after April 5th. The results are dominated by the simulations of April 5th-20th. We checked the results averaged

for April 5th-20th, and the difference is quite small from the averages for April 1st-20th.

- *5. I agree that wind change due to topography is one key factor affecting BC transport in the region. However, another important factor that was not discussed/analyzed by the authors is how the cloud and precipitation fields change due to the topographic difference in their model simulations, which could affect aerosol wet deposition and further the amount of BC transported to the TP. This also seems to be a confounding factor for wind analysis. I suggest at least including some discussions on this aspect.*

Thank you for your suggestion. In fact, we did include some analysis of precipitation difference due to the topographic effect as shown in Figure S10. The results were discussed in Section 3.3.

As our response to the comment above, the wet deposition is included in our simulation, however, we didn't emphasize this process because its impact is quite small during our simulation period. During the pre-monsoon season, precipitation over the region to the south of Himalayas is quite small (Fig. S10). Along the Himalayas and over the TP, the precipitation is relatively large. We have discussed in the manuscript that, based on our analysis of the contribution of each model process (transport, dry-deposition, emission, PBL mixing, and wet deposition) to the increase of BC column mass averaged over the TP during the simulation period, the two main processes affecting the BC column mass over the TP during the period are transport and dry deposition. The impact of wet deposition is different between the two experiments with different topography, however, the difference is much smaller than that of transport (source) and dry deposition (sink). That's why we didn't emphasize the analysis of wet deposition impacts. We have clarified this in the manuscript as

"Although the impacts of PBL mixing and wet deposition on the BC column mass over the TP are also different between the simulations with different topography, their impacts are much smaller than those of transport and dry deposition during the study period."

One reason of relatively small impact of wet deposition may be because of inactive convection during the pre-monsoon season. We have discussed in the manuscript that the aerosol-climate interaction with the consideration of complex topography during the monsoon season deserves further investigation, as following:

"In addition, the active convection during the monsoon season may also play an important role on pollutant transport across the Himalayas, which deserves further investigation. Furthermore, aerosol impact on cloud and precipitation, particularly during the monsoon season, and thus on the latent heat in the atmosphere and the

associated responses may also depend on the complex topography."

- ***6. In the analysis of wind and transport, the authors mainly focused on the near-surface wind (within PBL) which is directly affected by topography. How about transport at a higher altitude? The topography changes near-surface BC concentrations and probably vertical transport to free troposphere over the source regions and on the way to the Himalayas. The changes in BC vertical profile will also alter BC transport in the free troposphere or even at a higher altitude, which may affect the total BC transport to the TP. Is this factor unimportant compared to near-surface transport? What is the relative importance of the high-altitude transport pathway and the near-surface valley-mountain transport pathway?***

Yes, the topography may also affect the vertical transport and hence the vertical profile of BC. In our simulation period, the changes of vertical profile (shape) of BC concentration are small due to the topographic effect (Fig. S9). This may be due to that in our simulation period, the convective transport is not active and the topographic impact on the PBL mixing is relatively small as we discussed in the manuscript.

To confirm this, we checked the transport fluxes of Fig. 14 at different altitudes above the ground of 0-2 km, 2-4 km, and 4 km and above. It shows that the transport flux below 2 km dominates (> 80%) the column integrated transport flux, which is consistent with that the BC concentration reduces significantly from surface to 4 km above the ground (Fig. S9). Although we showed the change of near-surface wind (below 500 m) in the manuscript, the change of wind below 2 km is consistent. In addition, we further checked that the topographic impact on the wind in the free troposphere (e.g., 4 km above the ground) is quite small. Therefore, we can conclude that the change of near-surface transport due to the topography is the main reason of different BC transport towards the TP in this study.

Now, in the revised manuscript, we add the clarification in the caption of Fig. 13 as "The results averaged within 2 km above the ground are consistent."

In Section 3.2, "The wind in free troposphere (4 km above the ground and above) is also examined, and the change due to the topography is relatively small (not shown).", and "The analysis of the transport fluxes at different altitudes indicates that the transport fluxes below 2 km (above the ground) dominate (> 80%) the total flux."

Impact of topography on black carbon transport to the southern Tibetan Plateau during pre-monsoon season and its climatic implication

[1]Meixin Zhang, [1]Chun Zhao*, [2,3]Zhiyuan Cong, [1]Qiuyan Du, [1]Mingyue Xu, [1]Yu Chen, [4]Ming Chen, [1]Rui Li, [1]Yunfei Fu, [1]Lei Zhong, [3,5]Shichang Kang, [6]Delong Zhao, [6]Yan Yang

[1]School of Earth and Space Sciences, University of Science and Technology of China, Hefei, China

[2]Key Laboratory of Tibetan Environment Changes and Land Surface Processes, Institute of Tibetan Plateau Research, Chinese Academy of Sciences (CAS), Beijing 100101, China

[3]CAS Center for Excellence in Tibetan Plateau Earth Sciences, Institute of Tibetan Plateau Research, CAS, Beijing 100101, China

[4]National Center for Atmospheric Research, Boulder, CO, USA

[5]State Key Laboratory of Cryosphere Science, Northwest Institute of Eco-Environment and Resources, CAS, Lanzhou 730000, China

[6]Beijing Weather Modification Office, Beijing 100101, China

*Corresponding author: Chun Zhao (chunzhao@ustc.edu.cn)

Key points:
1. The black carbon (BC) transport across the Himalayas can overcome a majority of mountain ridges, but the valley transport is much more efficient during the pre-monsoon season.
2. The complex topography results in stronger overall crossing-Himalayas transport during the study period primarily due to the strengthened efficiency of near-surface meridional transport towards the TP, enhanced wind speed at some valleys, and deeper valley channels associated with larger transported BC mass volume.
3. The complex topography generates 50% higher transport flux of BC across the Himalayas and 30-50% stronger BC radiative heating in the atmosphere up to 10 km over the Tibetan Plateau (TP) than that with the smoother topography, which implies that the smooth topography used by global climate models with relatively coarse resolution may introduce significant negative biases in estimating BC radiative forcing over the TP due to smooth topography during the pre-monsoon season.
4. The different topography also leads to different distributions of snow cover and BC forcing in snow over the TP.

Abstract

Most of previous modeling studies about black carbon (BC) transport and impact over the Tibetan Plateau (TP) conducted simulations with horizontal resolutions coarser than 10 km that may not be able to resolve well the complex topography of the Himalayas. In this study, the two experiments covering entire Himalayas with the Weather Research and Forecasting Model coupled with chemistry (WRF-Chem) at the horizontal resolution of 4 km but with two different topography datasets (4-km complex topography and 20-km smooth topography) are conducted for pre-monsoon season (April, 2016) to investigate the impacts of topography on modeling the transport and distribution of BC over the TP. Both experiments show evident accumulation of aerosols near the southern Himalayas during the pre-monsoon season, consistent with the satellite retrievals. The observed episode of high surface BC concentration at the station near the Mt. Everest due to heavy biomass burning near the southern Himalayas is well captured by the simulations. The simulations indicate that the prevailing up-flow across the Himalayas driven by the large-scale westerly and small-scale southerly circulations during the daytime is the dominant transport mechanism of South Asian BC into the TP, and is much stronger than that during the nighttime. The simulation with 4-km topography resolves more valleys and mountain ridges, and shows that the BC transport across the Himalayas can overcome a majority of mountain ridges but the valley transport is more efficient. The complex topography results in stronger overall crossing-Himalayas transport during the simulation period primarily due to the strengthened efficiency of near-surface meridional transport towards the TP, enhanced wind speed at some valleys, and deeper valley channels associated with larger transported BC mass volume. This results in 50% higher transport flux of BC across the Himalayas and 30-50% stronger BC radiative heating in the atmosphere up to 10 km over the TP from the simulation with 4-km complex topography than that with 20-km smoother topography. The different topography also leads to different distributions of snow cover and BC forcing in snow. This study implies that the smoother topography used by global climate models generally with even coarser resolutions than 20 km and therefore relatively smoother topography may introduce significant negative biases in estimating light absorbing aerosol radiative forcing over the TP during the pre-monsoon season.

6

1. Introduction

The Tibetan Plateau (TP) is the highest plateau in the world with an average elevation over 4 km and an area of approximately 2.5×10^6 km^2, known as the world's third pole (Qiu, 2008), and its enormous dynamic and thermal effects have a huge impact on large-scale atmospheric circulation through the energy exchange with the atmosphere especially the troposphere, such as Asian monsoon (e.g., Ye and Wu, 1998; Duan and Wu, 2005; Wu et al., 2007, 2012a; Boos and Kuang, 2013; Chen and Bordoni, 2014; He et al., 2019; Zhao et al., 2019). In addition, the glacial melting water of TP is one of the important sources of water resources of the Indus River, Ganges River, Yangtze River, and Yellow River in Asia (e.g., Singh and Bengtsson, 2004; Barnett et al., 2005; Immerzeel et al., 2010; Lutz et al., 2014). Previous studies found aerosols in the atmosphere over/around the TP could change the regional climate of Asia (e.g., Qian et al., 2011, 2015; Lau et al., 2017, 2018). Model simulations showed that the absorptive aerosols changed the surface radiative flux over the TP by 5-25 W m^{-2} during the pre-monsoon season in April and May and led to the changes in summer monsoon circulations (Qian et al., 2011). Meanwhile, aerosol may affect the atmosphere by modulating the vertical structure of cloud and precipitation around the TP, and thus change the distribution of atmospheric latent heat around the TP, which is the main driving force of regional atmosphere circulations (e.g., Li et al., 2010, 2017, 2019). Moreover, when absorbing aerosols settle on the snow-covered areas, they will blacken the surface of snow cover and glacier to a large extent (e.g., Hansen and Nazarenko, 2004; Ramanathan and Carmichael, 2008; Lau et al., 2010, 2018; Lee et al., 2013; Zhang et al., 2017, 2018), reduce the snow albedo so as to absorb more solar radiation and cause the consequences of accelerated melting (e.g., Ramanathan et al., 2007; Ming et al., 2009; Yasunari et al., 2010; Ji et al., 2015; Zhang et al., 2015). According to the Intergovernmental Panel on Climate Change Fifth Assessment Report (IPCC AR5), the radiative forcing caused by the important component of absorbing aerosols, black carbon (BC), on the surface snow is 0.04 W m^{-2} (0.02-0.09 W m^{-2}) on global average, and the regional forcing (such as over the Arctic and the Himalayas) can be considerably large.

The TP is surrounded by various sources of pollutants. Over the South of TP, previous studies have suggested that South Asia was the main source of pollutants transported to the plateau (e.g., Cong et al., 2009, 2015a, b; Kopacz et al., 2011; Lu et al., 2012; Zhao et al., 2013; Wang et al., 2015; Zhang et al., 2015; Kang et al., 2016, 2019; Li et al., 2016; Chen et al., 2018). A huge blanket or layer of "haze" composes of light-absorbing carbonaceous aerosol

107 particles that often erupts in the pre-monsoon season over South Asia and has a significant
108 influence on the plateau (e.g., Prasad and Singh, 2007; Engling and Gelencser, 2010). Among
109 them, biomass burning emission reaching the maximum in pre-monsoon season over South
110 Asia is one of the dominant sources (e.g., Cong et al., 2015b). Many studies investigated the
111 transport mechanisms of South Asian pollutants to the TP and found that the pollutants
112 transported across the Himalayas were mainly due to the combination of large-scale circulation
113 and regional wind (e.g., Hindman and Upadhyay, 2002; Cao et al., 2010; Dumka et al., 2010;
114 Marinoni et al., 2010; Cong et al., 2015a; Kang et al., 2016; Lüthi et al., 2015; Zhang et al.,
115 2017). Cong et al. (2015b) suggested that strong large-scale westerly and local small-scale
116 mountain-valley wind passed through western Nepal, northwest India and Pakistan (i.e.,
117 southern Himalayas) in the pre-monsoon season. Dumka et al. (2010) and Kang et al. (2016)
118 inferred from the trajectory analysis that long-distance transport from Africa and Europe may
119 also affect the BC concentration of Himalayas in addition to the influence of regional pollution.
120 The synoptic troughs and ridges were also found favoring the transport of pollutants into the
121 TP from South Asia (Lüthi et al., 2015).

122 Although previous studies have confirmed the transport of pollutants across the Himalayas,
123 the complex topography of Himalayas complicates transport mechanisms. On one hand, Cao
124 et al. (2010) revealed that the Himalayas acted as a huge barrier to the transport of a large
125 amount of BC over the plateau based on model simulations. On the other hand, some studies
126 found that the valleys across the Himalayas served as channels for efficient transport of
127 pollutants (e.g., Hindman and Upadhyay, 2002; Marinoni et al., 2010). Marinoni et al. (2010)
128 analyzed the observation of wind at a station of the southern Himalayas and found that a distinct
129 valley wind system with the prominent southerly continuously transported pollutants to the
130 plateau. Most of these studies used observations and back-trajectory models to demonstrate the
131 transport pathways of pollutants to the TP, which cannot explicitly reveal the transport
132 mechanisms underneath, in particular quantifying the impacts of complex topography.

133 A few of modeling studies investigated the pollutant transport mechanisms using 3-D
134 chemical transport models (e.g., Kopacz et al., 2011; Liu et al., 2015; Zhang et al., 2017; Yang
135 et al., 2018). However, most of them simulated transport processes at relatively coarse
136 horizontal resolutions (e.g., 20-100 km), which cannot resolve well the complex topography of
137 Himalayas. It is noteworthy that studies about the aerosol climatic impact over the TP also used
138 climate models at relatively coarse horizontal resolutions (e.g., Flanner and Zender, 2005;
139 Menon et al., 2010; Kopacz et al., 2011; Qian et al., 2011, 2015; He et al., 2014; Zhang et al.,
140 2015; Ji et al., 2016). So far, there is only one study that used a chemical transport model at a

horizontal resolution of sub-10 km to investigate pollutant transport mechanisms over the eastern Himalayas (Cao et al., 2010). Furthermore, none of studies assessed quantitatively the impacts of topography on modeling the pollutant transport across the Himalayas and hence on estimating aerosol distribution and radiative forcing over the TP.

In order to examine the potential impacts of complex topography on pollutant transport across the Himalayas over the TP, this study conducts multiple experiments with the Weather Research and Forecasting Model coupled with chemistry (WRF-Chem, Grell et al., 2005; Skamarock et al., 2008). The WRF-Chem model is selected because it includes the interaction between meteorology and aerosol and is widely used for regional modeling of aerosol and its climatic impact (e.g., Cao et al., 2010; Zhao et al., 2010, 2011, 2012, 2014; Wu et al., 2013; Gao et al., 2014; Huang et al., 2015; Fan et al., 2015; Feng et al., 2016; Zhong et al., 2017; Sarangi et al., 2019; Liu et al., 2020). The model has also been used to investigate the aerosol transport and climatic impact over the Himalayas region (e.g., Feng et al., 2016; Cao et al., 2010; Sarangi et al., 2019). The model is suitable for simulations at hydrostatic and non-hydrostatic scales and thus can be used for investigating the impacts of resolution-dependent feature, such as topography, on modeling results. In particular, the meteorological part of the model (WRF) has been systematically evaluated and used to investigate the impacts of resolutions on simulations of moisture transport and climate over the Himalayas region (e.g., Shi et al., 2008; Karki et al., 2017; Lin et al., 2018; Zhou et al., 2017, 2018; Wang et al., 2020). All of these previous studies with the model lay the foundation for this modeling study.

Two experiments with different topography representations are conducted to investigate the impacts of topography complexity on the pollutant transport across the Himalayas and the resulting radiative forcing over the TP. The simulations are conducted for April 2016 in pre-monsoon season, because South Asia is seriously polluted during this period and the pollutants transported to the TP during the period may have significant impacts on Asian monsoon system (e.g., Lau et al., 2006a, b; Ding et al., 2009; Kuhlmann and Quaas, 2010; Qian et al., 2011, 2015). In addition, the observed concentration of BC at the observation station besides Mt. Everest shows an evident pollution episode from April 5th to 16th of 2016, deserving the investigation of the transport mechanisms. The rest of the paper is organized as follows. Section 2 describes briefly the WRF-Chem model, the physics parameterizations, and the model configuration for this study, followed by a description of data for evaluation. The series of numerical experiments at different resolutions are analyzed in Section 3. The findings are then summarized and discussed in Section 4 and 5.

2. Methodology

2.1 Model and experiments

2.1.1 WRF-Chem model

In this study, the version of WRF-Chem updated by University of Science and Technology of China (USTC version of WRF-Chem) is used. This USTC version of WRF-Chem includes some additional capabilities such as the diagnosis of radiative forcing of aerosol species, land surface coupled biogenic volatile organic compound (VOC) emission, aerosol-snow interaction compared with the publicly released version (Zhao et al., 2013a, b, 2014, 2016; Hu et al., 2019; Du et al., 2020). The Model for Simulating Aerosol Interactions and Chemistry (MOSIAC) (Zaveri et al., 2008) and the Carbon Bond Mechanism-Z (CBM-Z) gas phase mechanisms (Zaveri and Peters, 1999) are selected. The MOSAIC aerosol scheme uses an approach of segmentation to represent aerosol size distribution with four or eight discrete size bins (Fast et al., 2006). It consists of a range of physical and chemical processes such as nucleation, condensation, coagulation, aqueous phase chemistry, and water uptake by aerosol. The parameterization of dry deposition of aerosol mass and number is according to the method of Binkowski and Shankar (1995), including particle diffusion and gravitational effects. Aerosol-cloud interactions were included in the model by Gustafson et al. (2007) for calculating the activation and re-suspension between dry aerosols and cloud droplets. The wet removal of grid-resolved stratiform clouds/precipitation includes two aspects, namely in-cloud removal (rainout) and below-cloud removal (washout) by Easter et al. (2004) and Chapman et al. (2009), respectively. Aerosol optical properties such as single scattering albedo (SSA) and scattering asymmetry and so on are calculated at each model grid through the function of wavelength. The shortwave (SW) and longwave (LW) refractive indices of aerosols use the Optical Properties of Aerosols and Clouds (OPAC) data set (Hess et al., 1998), with a detailed description of the computation of aerosol optical properties can be found in Barnard et al. (2010) and Zhao et al. (2013a). For both short wave and long wave radiation, aerosol radiation feedback combined with the Rapid Radiative Transfer Model (RRTMG) (Mlawer et al., 1997; Iacono et al., 2000) was implemented by Zhao et al. (2011). For the diagnosis of the optical properties and direct radiative forcing of various aerosol species in the atmosphere, the method described by Zhao et al (2013a) is adopted. The radiative forcing of light absorbing aerosol in surface snow is estimated with the Snow, Ice, and Aerosol Radiative model (SNICAR) (Flanner and Zender, 2005) in the land surface scheme as introduced by Zhao et al. (2014). Please note that the SNICAR model was recently updated by He et al. (2018) to include the

208 <u>impact of non-spherical snow grains on aerosol snow-albedo effect that is not included in this</u>

209 <u>study.</u> More details about the coupling between the WRF-Chem and SNICAR models can be

210 found in Zhao et al. (2014).

211

212 2.1.2 Numerical experiments

213   In this study, the WRF-Chem simulations are performed with two nested domains (one-

214 way nesting), one outer domain at 20-km horizontal resolution with 350×250 grid cells (62°E

215 -112°E, 1°N -38°N) and one inner domain at 4-km horizontal resolution with 400×300 grid

216 cells (75°E -92°E, 23°N -35°N) (Fig. 1). The inner domain roughly covers the entire Himalayas.

217 The WRF-Chem simulations conducted in this study use the terrain following coordinate

218 (Skamarock et al., 2008). To resolve the vertical structure of transport across the Himalayas,

219 the simulations are configured with 54 vertical layers and denser layers near the surface. For

220 example, averaged over a region (26°N-28°N, 76°E-80°E) near the southern Himalayas, there

221 are about 17 layers below 2 km above the ground (Fig. 2). The goal of this study is to investigate

222 the impacts of different representations of topography on the transport of BC across the

223 Himalayas. Therefore, besides this control experiment, one sensitivity (idealized) experiment

224 is also conducted with the same configuration as the control one except that the terrain heights

225 of the inner domain at 4-km resolution are bilinearly interpolated from the terrain heights at

226 20-km resolution similar as previous studies (e.g., Shi et al., 2008; Wu et al., 2012b; Lin et al.,

227 2018). The two experiments are referred to the simulations with complex and smooth

228 topography, respectively, hereafter.

229   Fig. 3 shows the spatial distribution of terrain height over the inner domain with complex

230 (4-km dataset) and smooth (20-km dataset) topography. It is evident that the terrain is much

231 smoother from the 20-km dataset than from the 4-km dataset. The mountain ridges and valleys

232 can be resolved to some extent in the 4-km dataset but mostly missed or underestimated at 20-

233 km. The probability distributions of terrain height over Himalayas from the 20-km and 4-km

234 datasets (Fig. S1 in the supporting material) show that the difference between the two datasets

235 is small for the terrain height lower than ~4.5 km but is significant for the terrain height above

236 ~4.5 km. In addition, the slopes between the neighboring grids are significantly reduced in

237 general with the smooth topography compared to with the complex topography, particularly

238 over the Himalayas region (Fig. S2 in the supporting material). The difference of results from

239 the two experiments over the inner domain is analyzed as the impacts of topography

240 representations. Therefore, all the results shown below are from the simulations of the inner

241 domain at 4-km resolution with different topography if not otherwise stated. It is noteworthy
242 that this study focuses on understanding the impact of complex topography resolved by 4 km
243 instead of the difference between 4-km and 20-km simulations. Prescribing the topography at
244 4 km following the 20-km resolution distribution is just one way to smooth the topography. In
245 fact, the sensitivity experiment at 4-km resolution with the topography from the one-degree
246 resolution dataset is also conducted, and the result is consistent. In addition, although the
247 topography at 4-km resolution resolves much better topography of Himalayas than that at 20-
248 km resolution, it still cannot fully resolve the complexity of topography of Himalayas. The
249 higher resolution (e.g., 1 km or sub-1 km) may be needed. Previous studies have found that the
250 simulations at the resolutions between 1 km and 4 km can produce generally consistent features,
251 but the simulation at 1 km with better representation of topography can produce a little better
252 meteorological field compared to the observations (e.g., Karki et al., 2017). One sensitivity
253 experiment at 1.5-km resolution is also conducted in this study and found the difference
254 between the simulations at 1.5-km and 4-km resolutions is relatively small. However, it should
255 be noted that the simulation at 1.5-km resolution is only conducted covering a much smaller
256 region for a shorter period due to the computational cost. The experiment at 4-km instead of
257 1.5-km resolution is conducted finally for the study region and period due to the balance of
258 resolving the complex topography to some extent and affordable computational cost.

259   The simulations are conducted for March 29th-April 20 of 2016 for the reason as discussed
260 in the introduction. The results of April 1th-20th are analyzed for the observed pollution episode
261 to allow a few days spin-up for chemical initial condition. The meteorological initial and lateral
262 boundary conditions are derived from the European Centre for Medium-Range Weather
263 Forecasts (ECMWF) reanalysis data at 0.5°×0.66° horizontal resolution and 6 h temporal
264 intervals (ERA-Interim dataset). The modeled u and v component wind, atmospheric
265 temperature, and geopotential height over the outer domain are nudged towards the reanalysis
266 data with a nudging timescale of 6 h following previous studies (e.g., Stauffer and Seaman,
267 1990; Seaman et al., 1995; Liu et al., 2012; Zhao et al., 2014; Karki et al., 2017; Hu et al., 2016,
268 2020). Spectral nudging method is applied to balance the performance of simulation at the large
269 and small scales (Liu et al., 2012), and only to the layers above the planetary boundary layer
270 (PBL) with nudging coefficients of 3×10^{-4} s^{-1}. A wave number of three is selected for both
271 south-north and west-east directions. Please note that the choices of nudging coefficients and
272 wave numbers for spectral nudging in this study are empirical. The purpose of nudging is to
273 simulate reasonably large-scale feature so that small-scale impacts from the complex

274 topography can be focused. Therefore, the modeling sensitivity to these choices is not tested in

275 this study. The results show that the simulations with nudging method can reproduce the large-

276 scale circulation at 700 hPa and higher over the outer domain compared to the reanalysis dataset

277 with the spatial correlation coefficient of 0.96-0.98.

278   The Mellor-Yamada-Nakanishi-Niino (MYNN) planetary boundary layer scheme

279 (Nakanishi and Niino, 2006), Community Land Model (CLM) land surface scheme (Oleson et

280 al., 2010), Morrison 2-moment microphysics scheme (Morrison et al., 2009), Kain-Fritsch

281 cumulus scheme (Kain, 2004), and Rapid Radiative Transfer Model (RRTMG) longwave and

282 shortwave radiation schemes (Iacono et al., 2000) are used in this study. It is noteworthy that

283 the cumulus scheme is only used in the outer domain at 20 km resolution and is turned off in

284 the inner domain at 4 km resolution. The chemical initial and boundary conditions are provided

285 by a quasi-global WRF-Chem simulation for the same time period to include long-range

286 transported chemical species. The quasi-global WRF-Chem simulation is performed at $1°×1°$

287 horizontal resolution using a quasi-global channel configuration with $360×130$ grid cells

288 ($180°W$-$180°E$, $60°S$-$70°N$). More details about the general configuration of quasi-global

289 WRF-Chem simulation can be found in Zhao et al. (2013b) and Hu et al. (2016). The detailed

290 configuration of WRF-Chem experiments is summarized in Table 1. Due to the lack of publicly

291 available in-situ observations, this study does not tend to evaluate systematically the simulated

292 meteorological fields over the Himalayas region. However, as shown in Table 1, the choice of

293 physical parameterizations in this study follows that of one previous study (Karki et al., 2017)

294 that evaluated systematically the WRF simulation for one entire year over the Himalayas region.

295 Their results showed that the WRF simulation at convection-permitting scale could generally

296 capture the essential features of meteorological fields such as precipitation, temperature, and

297 wind over the Himalayas region. Therefore, the WRF-Chem simulations in this study are

298 reliable to investigate the impacts of topography over the Himalayas region.

299

300 2.1.3 Emissions

301   Anthropogenic emissions for outer and inner simulation domains are obtained from the

302 Hemispheric Transport of Air Pollution version-2 (HTAPv2) at $0.1°×0.1°$ horizontal resolution

303 and a monthly temporal resolution for year 2010 (Janssens-Maenhout et al., 2015), except that

304 emissions of East Asia are from the MIX Asian anthropogenic emission inventory at $0.1°×0.1°$

305 horizontal resolution for 2015 (Li et al., 2017). Biomass burning emissions are obtained from

306 the Fire Inventory from National Center for Atmospheric Research (FINN) with hourly

307 temporal resolution and 1-km horizontal resolution (Wiedinmyer et al., 2011) for the
308 simulation period, and are vertically distributed following the injection heights suggested by
309 Dentener et al. (2006) from the Aerosol Comparison between Observations and Models
310 (AeroCom) project. Sea-salt emission follows Zhao et al. (2013b), which includes correction
311 of particles with radius less than 0.2 μm (Gong, 2003) and dependence of sea-salt emission on
312 sea surface temperature (Jaeglé et al., 2011). The vertical dust fluxes are calculated with the
313 Georgia Tech/Goddard Global Ozone Chemistry Aerosol Radiation and Transport (GOCART)
314 dust emission scheme (Ginoux et al., 2001), and the emitted dust particles are distributed into
315 the MOSAIC aerosol size bins following a theoretical expression based on the physics of scale-
316 invariant fragmentation of brittle materials derived by Kok (2011). More details about the dust
317 emission scheme coupled with MOSAIC aerosol scheme in WRF-Chem can be found in Zhao
318 et al. (2010, 2013b).

319   As shown in Fig. 1, anthropogenic fossil fuel emissions of BC are high over Northeast
320 India. The fossil fuel BC emissions over Nepal, the country nearby the southern Himalayas,
321 are relatively low. Instead, biomass burning emissions of BC are extremely high in Nepal and
322 Northwest India (South Himalayas, 26°N-29°N). Averaged over the South Himalayas of inner
323 domain that may significantly affect the pollutant transport into the TP, the biomass burning
324 emissions of BC are much higher than its anthropogenic fossil fuel emissions, particularly for
325 the pollution episode (Fig. 4). The anthropogenic BC emissions are set constant through April,
326 while biomass burning emissions show a strong fire event in April 5-16. During the event, the
327 biomass burning BC emissions can be a factor of 2 of the anthropogenic fossil fuel BC
328 emissions over South Himalayas.
329
330 **2.2 Dataset**
331   Three datasets are used to compare with the modeling results to demonstrate the pollutant
332 episode and spatial distribution. One is from the Moderate Resolution Imaging
333 Spectroradiometer (MODIS) instruments on Aqua and Terra satellites. The MODIS Aerosol
334 Product monitors the ambient aerosol optical thickness over the oceans globally and over the
335 continents. Daily Level 2 Aerosol Optical Depth (AOD) at 550 nm products with the spatial
336 resolution of 10 km×10 km (at nadir) from both Aqua and Terra are applied. When compared
337 with the modeling results, the simulations are sampled at the satellite overpass time and
338 location. The second one is from the Aerosol Robotic Network (AERONET) (Holben et al.,
339 1998) that has ~100 similar globally distributed sun and sky scanning ground-based automated
340 radiometers, which provide measurements of aerosol optical properties throughout the world

341 (Dubovik and King, 2000; Dubovik et al., 2002). In this study, AERONET measured AOD at

342 675 nm and 440 nm from two sites over the TP, QOMS_CAS site (86.95°E, 28.36°N) and

343 NAM_CO site (90.96°E, 30.77°N) are used to derive the AOD at 550 nm (using the Angström

344 exponent) for comparison with modeling results at 550 nm. All of the retrievals of AOD are at

345 quality level 2, and the uncertainty of AOD measurements is about 0.01 (Holben et al., 2001).

346 In this study, the available data in April 2016 are used to evaluate the modeling results during

347 the same period.

348   The third one is the measurement of surface BC mass concentration collected during the

349 simulation period for April 4-20 of 2016 at the Qomolangma Station for Atmospheric and

350 Environmental Observation and Research (QOMS, 86.95°E, 28.36°N) which is located at the

351 northern slope of the Mt. Everest, about 4276 meters above sea level. The BC mass

352 concentration is measured with the widely-used instrument Aethalometer (AE-33) that can

353 provide real-time BC mass concentration measurements. The calibration of air flow is routinely

354 conducted to maintain the data quality. The instrument estimates the BC mass concentration

355 based on the optical method through measuring the reduction in light intensity induced by BC.

356 The method assumes that the relationship between attenuation and BC surface loading is linear

357 for low attenuation values. However, this relationship becomes nonlinear when the attenuation

358 values are high due to a filter saturation effect, which may lead to underestimation of the high

359 BC concentration. The detection limit of AE-33 instrument is 5 ng/m^3, and the uncertainty is

360 estimated to be within 10% (e.g., Chen et al., 2018; Bansal et al., 2019; Kant et al., 2019). The

361 dataset of BC mass concentration used in this study was reported by Chen et al., (2018), where

362 more details about the measurements can be found.

363

3. Results

3.1 Spatial distribution of BC around the TP

366   Figure 5 shows the spatial distributions of column integrated BC mass within the inner

367 domain from the simulations at 4-km resolution with complex and smooth topography

368 averaged for April 1-20, 2016, and the difference between the two is also shown. For both

369 experiments, the Himalayas is an apparent boundary line for the distribution of BC with a sharp

370 gradient across the Himalayas. The high BC mass loading exists near the southern Himalayas

371 reaching over 10 mg/m^2, which is largely contributed by the biomass burning emissions during

372 the period (Fig. 4), while the value reduces significantly to less than 0.4 mg/m^2 over the TP.

373 The BC mass loading near the central and eastern Himalayas is higher than that near the

374   western Himalayas. In general, the column BC mass loading from the simulation with complex

375   topography is higher over the TP and lower over the region to the south of Himalayas compared

376   with the smooth topography, reflecting the stronger transport of BC from the source region to

377   the Himalayas and TP due to the complex topography (see the discussion in Section 3.2). Figure

378   6 displays the spatial distributions of AOD from the MODIS retrievals and the simulations at

379   4 km with two different topography averaged for April 1-20, 2016. In general, both simulations

380   reproduce the overall spatial distribution of AOD, with the large values near the southern

381   Himalayas, consistent with the BC mass loading. In addition, both the simulations and satellite

382   retrievals show higher AOD near the central and eastern Himalayas than that near the western

383   Himalayas during the study period. The difference between the simulations and retrievals may

384   be partly related to the uncertainties in emissions particularly for biomass burning emissions.

385   Other than intense emissions, the wind circulation around the TP may also play an important

386   role in accumulating BC near the southern Himalayas. Because of the block of Himalayas, the

387   wind circulation at 500 hPa is divided into two branches as westerly and northwesterly. Both

388   of them are relatively dry airflows with little effect on pollutant removal, favor the

389   accumulation of pollutants near the southern Himalayas, and carry the pollutants to the TP (e.g.,

390   Dumka et al., 2010; Kang et al., 2016; Cong et al., 2015a).

391   The AOD retrieved at two AERONET sites over the TP are compared with the two

392   simulations for April 1-20, 2016 (Fig. 7). The AOD at the QOMS_CAS site near the northern

393   Himalayas is higher than that at the NAM_CO site inside of the TP. Both simulations can

394   capture this gradient. The simulation with complex topography produces higher AOD than

395   does the one with smooth topography at both sites. The modeling biases (normalized mean bias,

396   NMB) reduce from -46% (smooth topography) to 9% (complex topography) at the

397   QOMS_CAS site and from -26% (smooth topography) to -10% (complex topography) at the

398   NAM_CO site. Although the correlation coefficient between the simulations and observation

399   increases from 0.37 (smooth topography) to 0.53 (complex topography) at the QOMS_CAS

400   site, it is similar (~0.2) between the two simulations at the NAM_CO site. The correlation

401   coefficient is higher at the QOMS_CAS site near the source region than the NAM_CO site

402   farther away, which may indicate the model processes affecting the transport over the TP still

403   need examination with more observations. The NAM_CO site over the eastern TP may also be

404   affected by other sources that are not counted in this study. The modeling of temporal variations

405   of pollutants over the TP deserves further investigation with more observations.

406   There is one in-situ observational station (QOMS) near the Mt. Everest (black dot shown

407   in Fig. 1) to collect the surface BC concentration. The observed surface BC concentration at

408 this station is compared with the corresponding simulations for this period as shown in Figure

409 8. Without local emission source, the surface BC concentration at QOMS is primarily

410 contributed by the transport. The temporal variation of observed surface BC concentration

411 correlates highly with the biomass burning emissions as shown in Fig. 4, with the peak value

412 on April 11 reaching ~3 ug/m^3. One sensitivity experiment without biomass burning emissions

413 shows that the simulated BC concentration at QOMS will be significantly reduced without the

414 peak (not shown), which further proves that the BC concentration over the northern Himalayas

415 can be largely influenced by the pollution episode near the southern Himalayas. It is noteworthy

416 that both simulations can reproduce the episode in time and magnitude, and the difference at

417 this station is small. The spatial distribution of difference in near-surface BC concentration

418 between the two simulations (Fig. S3) is more heterogeneous than that of column BC mass

419 (Fig. 5), reflecting the impact of topography on near-surface transport (see the discussion in

420 Section 3.2).

421

3.2 Transport flux into the TP

423 To further understand the difference in BC surface concentration and column mass loading

424 over the TP between the two simulations with different topography, Figure 9 shows the

425 longitude-height cross section of BC transport flux along the cross line (shown as the black

426 dash line in Fig. 3) from the two simulations at local time (LT) 03:00 and 15:00 averaged for

427 April 1-20 to represent nighttime and daytime transport, respectively. The PBL height along

428 the cross line is also shown as the black dash line. The transport flux is calculated by projecting

429 the wind field perpendicularly to the cross line and then multiplying the BC mass concentration

430 along the cross line. More specifically, the transport flux is calculated as following:

431 $$\text{TF} = C * (u * \sin\alpha + v * \sin\beta) \qquad (1)$$

432 Where α is the angle between east-west wind component and the cross line, β is the angle

433 between south-north wind component and the cross line, and C is the BC mass concentration

434 at the grid along the cross line. The flux is estimated at each model level. Positive values

435 represent the transport towards the TP, while negative values represent the transport away from

436 the TP. It is evident that BC is imported into the TP during the day and night on the west of

437 ~85°E, although the transport flux is much larger during the daytime than nighttime. On the

438 east of ~85°E, BC is imported into the TP during the day but exported slightly from the TP

439 during the night. The difference of transport flux between the western and eastern Himalayas

440 is primarily due to the influence of large-scale westerly that is weak over the eastern Himalayas

441 (Fig. 5). The transport across the western Himalayas is controlled by the large-scale westerly,
442 while local southerly dominates the transport across the eastern Himalayas and also influences
443 the transport across the central Himalayas (Fig. S4 in the supporting material). The stronger
444 diurnal variation of local southerly (towards the TP in the daytime to away from the TP in the
445 nighttime) than that of westerly near the surface (Fig. S4) leads to the large difference in diurnal
446 variation of transport between the western and eastern Himalayas. The strong transport is
447 primarily within the PBL during the daytime, and the deeper PBL during the daytime allows
448 BC over the source region mixed to higher altitude, which also leads to stronger import
449 transport during the day than the night. The relatively small difference in simulated PBL
450 heights and structure between the two experiments can be due to their different surface heating
451 resulted from different topography complexity (e.g., Wagner et al., 2014).

452   The difference between the simulations with two different topography is evident. The
453 mountain ridges are much higher and valleys are much deeper with the complex topography
454 than with the smooth topography. The simulation with smooth topography produces
455 overwhelming crossing-Himalayas transport towards the TP within the PBL, in particular
456 during the daytime. Although, in the simulation with complex topography, the mountain ridges
457 resolved weaken the crossing-Himalayas transport compared to the simulation with smooth
458 topography, the overall positive values near the surface indicate that the transport can overcome
459 most mountain ridges along the Himalayas. The transport fluxes near the surface from the
460 simulation with complex topography become close-to-zero only at a few mountain ridges that
461 are 6.5 km or higher. To better demonstrate the transport pathway across mountain ridges, one
462 cross-section across the mountain ridge as shown as one black solid line in Fig. 3 is taken as
463 one example. Figure 10 shows the latitude-height cross section of BC mass concentration and
464 transport flux across one mountain ridge from the simulations with complex and smooth
465 topography at local time (LT) 03:00 and 15:00 averaged for April 1-20, 2016. Near the southern
466 part of mountain, the elevated concentration of BC mass accumulates and can mix up reaching
467 as high as 5 km with the much stronger transport during the daytime. It is obvious that the
468 mountain ridge in the simulation with smooth topography is quite low. With the high mountain
469 ridge resolved by the complex topography, the simulated BC transport flux can still cross the
470 mountain. Analysis of transport flux across a few more mountain ridges indicates similar
471 results (not shown). The results above indicate that the transport of pollutants can cross a
472 majority of mountain ridges of Himalayas, which is consistent with the observation-based
473 estimate by Gong et al. (2019) that also found pollutants could overcome the blocking effect
474 of mountain ridges of Himalayas as a transport pathway. On the other hand, the resolved deeper

475   valleys in the simulation with complex topography enhance the transport flux compared to the

476   one with the smooth topography. Similarly, Figure 11 shows one example of latitude-height

477   cross section of BC mass concentration and transport flux across one valley from the

478   simulations with complex and smooth topography at local time (LT) 03:00 and 15:00 averaged

479   for April 1-20, 2016. The transport is much stronger and deeper along the valley from the

480   simulation with complex topography than the one with smooth topography. Again, analysis of

481   transport flux across a few more valleys does not show different results (not shown).

482   In order to further demonstrate the overall inflow flux across the Himalayas, the vertically

483   integrated BC mass flux along the longitudinal cross section (as shown in Fig. 9) from the

484   simulations with different topography is shown in Figure 12. The terrain heights from the two

485   simulations along the cross section are also shown as black lines. The total mass flux is

486   calculated by integrating the right-hand term of equation (1) as following:

487    $$\text{ITF} = \int_{z=z_{sfc}}^{z=z_{top}} \delta z * C * (u * \sin\alpha + v * \sin\beta) \qquad (2)$$

488   Where δz is the thickness of each vertical model level. Similarly, positive values represent

489   the transport towards the TP, while negative values represent the transport away from the TP.

490   More evidently, the positive BC inflows towards the TP occur not only through the valleys but

491   also across the mountain ridges with both topography. The negative values only exist to the

492   east of 88°E. With complex topography, higher mountain ridges can reduce the transport flux

493   to some extent compared to the smooth topography. The complex topography results in

494   significantly larger BC inflow towards the TP compared to the smooth topography, particularly

495   corresponding to the deep valleys, such as the Karnali River Valley around 82°E and the Kali

496   Gandaki Valley around 84°E.

497   One reason for the enhanced transport across the Himalayas with the complex topography

498   is the resolved deeper valleys that lead to the increased valley wind. The wind across some

499   valleys can be significantly larger with the complex topography than the smooth one (Fig. S4).

500   The enhanced valley wind across the Himalayas has also been found by previous studies with

501   observations and numerical simulations (e.g., Egger et al., 2000; Zängl et al., 2001; Carrera et

502   al., 2009; Karki et al., 2017; Lin et al., 2018). However, it is noteworthy that previous studies

503   have found that the orographic drag (including gravity wave drag and turbulence orographic

504   form drag) over the region with complex topography, such as the Himalayas and other

505   mountainous areas, would weaken the overall near-surface wind speed (e.g., Beljaars et al.,

506   2004; Horvath et al., 2012; Jiménez and Dudhia, 2012; Zhou et al., 2017, 2018; Lin et al., 2018;

507   Wang et al, 2020). Therefore, the near-surface wind speed is also examined. The complex

508   topography does lead to the overall reduction of near-surface wind speed over the Himalayas

509   area (Fig. S5 in the supporting material), which is consistent with previous studies. However,

510   it is interesting to note that the near-surface southerly wind during the daytime of the simulation

511   period is overall increased over the Himalayas area with the complex topography (Fig. 13),

512   which indicates that the transport towards the TP is strengthened with the complex topography

513   in the daytime, particularly over the central and eastern Himalayas where the BC mass loading

514   is higher (Fig. 5). During the night, the meridional wind is dominated by northerly over the

515   Himalayas region in the simulation with the smooth topography. The complex topography

516   weakens the transport away from the TP or change the wind direction from northerly to

517   southerly over some areas of Himalayas. Both effects enhance the overall transport efficiency

518   across the Himalayas towards the TP. Therefore, although the complex topography weakens

519   the overall near-surface wind speed around the Himalayas, it induces more realistic small-scale

520   mountain-valley circulation that favors the BC transport across the Himalayas towards TP

521   during the study period. The wind in free troposphere (4 km above the ground and above) is

522   also examined, and the change due to the topography is relatively small (not shown). Another

523   effect of resolving valleys is that the volume of relatively-high-concentration BC could be

524   higher with deeper valleys (Fig. S6 in the support material), which can also result in stronger

525   transport towards the TP even if the wind condition is similar. For example, the altitude (above

526   the ground) below which the BC mass concentration is larger than $0.3/ug\ m^3$ is much higher

527   along the valleys with the complex topography than with the smooth topography (Fig. S7 in

528   the support material). The correlation coefficient between the difference of terrain heights of

529   valleys and of volumes of relatively-high-concentration BC can reach -0.76, indicating that the

530   lower the valleys are, the higher the volumes of BC mass can be transported across the

531   Himalayas. The combined influence of these factors results in significantly enhanced BC

532   transport towards the TP with the complex topography (Fig. 12), which can also be

533   demonstrated by the distributions of wind and BC mass concentration along the longitudinal

534   cross section (Fig. S8a, b in the support material).

535   The enhanced transport across the Himalayas turns out that the overall BC inflow with the

536   complex topography is much stronger than that with the smooth topography. Figure 14 shows

537   the accumulated integrated total transport flux of BC across the Himalayas estimated from the

538   simulations with complex and smooth topography for April 1-20, 2016. The accumulated

539   import flux of BC increases during the period in both experiments, and the difference between

540   the two experiments gradually increases with the time. At the end of period, the simulation

541   with complex topography estimates a total import flux of BC of $\sim1.5\times10^4$ Ton that is $\sim50\%$

542   higher than $\sim1.0\times10^4$ Ton estimated based on the simulation with smooth topography. The

543   analysis of the transport fluxes at different altitudes indicates that the transport fluxes below 2

544   km (above the ground) dominate ($>80\%$) the total flux. The sensitivity analysis by moving the

545   cross line (cross-section of the analysis in Fig. 9, 12, 14) towards or away from the TP within

546   a certain distance and re-calculating the flux indicates that the impacts of topography on the

547   simulated results do not change significantly.

548   All the analysis above focuses on investigating the BC transport flux across the Himalayas.

549   Although the inflow can reflect the impact of transport on the BC mass over the TP to some

550   extent, the change of BC mass concentration is eventually determined by the convergence of

551   transport. Therefore, the contribution of each model process (transport, dry-deposition,

552   emission, PBL mixing, and wet deposition) to the increase of BC column mass averaged over

553   the TP (with elevation >4 km) during this episode is analyzed for both simulations following

554   the methodology introduced by Du et al. (2020). The results show that the two main processes

555   affecting the BC column mass over the TP during the period are transport and dry deposition.

556   The transport is the dominant process that increases the BC column mass over the TP, while

557   the dry deposition reduces it. The contribution of transport to the increase of BC column mass

558   over the TP during the episode from the simulation with complex topography is significantly

559   larger than that with the smooth topography, which is consistent with the results shown by

560   analyzing the transport flux across the Himalayas. Although the impacts of PBL mixing and

561   wet deposition on the BC column mass over the TP are also different between the simulations

562   with different topography, their impacts are much smaller than those of transport and dry

563   deposition during the study period.

564

565   **3.3 Radiative forcing of BC over the TP**

566   The BC transported over the TP could significantly influence the regional climate and

567   water resources over Asia through heating the atmosphere and accelerating the melting of snow

568   and glacier (e.g., Qian et al., 2011, 2015; Lau et al., 2017). Therefore, the impact of the complex

569   topography on estimating the BC radiative heating profile in the atmosphere and radiative

570   forcing in surface snow deserves investigation. Figure 15 shows the vertical profiles of BC

571   induced radiative heating rate in the atmosphere averaged over the TP (with elevation >4 km)

572   within the inner domain shown in Fig.1 for April 1-20, 2016 from the simulations with complex

573   and smooth topography. Both simulations generate higher BC heating rate near the surface and

574 the rate gradually decreases with altitude, which is consistent with the vertical profiles of BC

575 mass concentration averaged over the TP (Fig. S9 in the supporting material). The BC heating

576 rate over the TP from the simulation with complex topography is ~0.17 K/day near the surface

577 and reduces to ~0.08 K/day at 8 km, which is ~50% and ~30%, respectively, higher than that

578 from the simulation with smooth topography at the corresponding altitudes. The higher BC

579 heating rate over the TP estimated by the simulation with complex topography is consistent

580 with its higher BC column mass (Fig. 5) and concentration profile (Fig. S9).

581   The BC radiative forcing in surface snow is controlled by both the distributions of BC

582 mass concentration and snow coverage (e.g., Zhao et al., 2014). Figure 16 shows the spatial

583 distributions of snow water equivalent (SWE) averaged for April 1-20, 2016 from the

584 simulations with two topography. The difference between the two is also shown. It shows that

585 the simulation with complex topography generates more areas with higher SWE compared to

586 that with the smooth topography over the TP. Along the Himalayas, the simulated SWE is

587 higher over the mountain ridges with the complex topography, particularly for the East

588 Himalayas, while the smooth topography leads to broader snow coverage over the West

589 Himalayas. The difference in SWE between the two simulations is highly correlated with their

590 difference in precipitation (Fig. S10 in the supporting material). Along the Himalayas, the

591 simulated precipitation with the complex topography is larger than that with the smooth

592 topography at the mountain ridges and smaller at the valleys. Over the TP, the overall

593 precipitation is larger with the complex topography than that with the smooth topography (Fig.

594 S10). Previous studies have found that the topography could significantly affect the

595 precipitation over the Himalayas region (e.g., Bookhagen and Burbank, 2010; Wulf et al., 2016;

596 Cannon et al., 2017; Karki et al., 2017).

597   Figure 17 shows the spatial distributions of BC radiative forcing in the surface snow over

598 the TP averaged for April 1-20, 2016 from the simulations with two topography, and the

599 difference between the two is also shown. The BC radiative forcing in surface snow is largely

600 coincident with the spatial distributions of SWE as shown in Fig. 16, mainly due to the

601 heterogeneous distributions of snow cover over the TP. The BC radiative forcing in surface

602 snow over the TP from the simulation with complex topography reaches 5 W/m^2 where the

603 snow exists, larger than that with the smooth topography. Along the Himalayas, the simulation

604 with complex topography produces higher BC snow forcing over the mountain ridges,

605 particularly over the eastern Himalayas, while the one with the smooth topography simulates

606 higher BC snow forcing over most areas of western Himalayas due to its broader snow

607 coverage there. Overall, the complex topography leads to higher BC forcing in snow over the

608   TP and the eastern Himalayas and lower BC forcing in snow over the western Himalayas, and

609   therefore results in the different distribution of BC forcing in snow over the TP and Himalayas,

610   compared to that with the smooth topography.

611

612   4. Summary

613   In this study, the model experiments with different topography are conducted to illustrate

614   the impacts of complexity of topography of Himalayas on BC transport from South Asia to the

615   TP. The observed pollution episode at the QOMS station besides the Mt. Everest during the

616   pre-monsoon season is simulated. The observed surface BC concentration shows a peak of ~3

617   ug/m^3 much larger than the background value of < 0.4 ug/m^3 over the TP. The observed

618   temporal variation of surface BC concentrations correlates highly with that of biomass burning

619   emissions near the southern Himalayas, indicating the significant impacts of biomass burning

620   on the pollutants over the TP. The simulations can reproduce the episode in time and magnitude,

621   and are used to investigate the BC transport mechanisms and the impacts of topography.

622   The high BC mass loading during the simulation period accumulates near the southern

623   Himalayas driven by the large-scale westerly and small-scale southerly circulations, which is

624   also observed by satellites. The modeling results demonstrate that the circulations favor the

625   accumulation of pollutants near the Himalayas, particularly the central and eastern parts, and

626   can carry the pollutants to the TP during the study period, which is consistent with previous

627   modeling studies (e.g., Kopacz et al., 2011). It is noteworthy that the BC accumulated near the

628   southern Himalayas can be transported across the Himalayas overcoming a majority of

629   mountain ridges, which is consistent with the observation-based estimate by Gong et al. (2019)

630   that also found pollutants could overcome the blocking effect of the mountain ridges of

631   Himalayas. However, the transport through the valleys is found much stronger and more

632   efficient than across the mountain ridges and the enhancement effect cannot be ignored. The

633   complex topography results in 50% higher overall transport flux across the Himalayas during

634   the simulation period than that with the smooth topography, primarily due to the strengthened

635   efficiency of near-surface meridional transport towards the TP, enhanced wind speed at some

636   valleys, and deeper valley channels associated with larger BC mass volume that can be

637   transported into the TP, although the overall wind speed is weakened due to the orographic

638   drags with the complex topography. This turns out that the simulation with complex

639   topography produces 30-50% higher BC radiative heating rate in the atmosphere up to 10 km

640   averaged over the TP than does the simulation with smooth topography.

For the BC radiative forcing in surface snow, the simulation with complex topography produces stronger forcing over the TP than that with the smooth one. The complex topography makes the distribution of BC forcing in surface snow quite different from the simulation with smooth topography, partly due to its different distribution of surface snow. The simulated BC radiative forcing in snow is distributed more heterogeneously than those in previous studies using global models at relatively coarse resolutions (e.g., Qian et al., 2011). He et al. (2014) used a global chemical transport model to simulate the BC forcing in snow at the horizontal resolution of ~0.2° and obtained the similar distribution as the simulation with smooth topography in this study with the high values over the western Himalayas. However, their simulated values near the Himalayas are higher than the simulated results of this study, which may be due to their estimation are averaged for November-April.

This study highlights the importance of resolving complex topography of the Himalayas in modeling the aerosol transport across the Himalayas and radiative impact over the TP. Although this study focuses on the impacts of topography on the simulated results, the additional analysis (Fig. S11-13 in the supporting material) of the outer domain simulation at 20-km resolution and the inner domain simulation at 4 km with different topography indicates that the resolution-dependent difference between 20 km and 4 km is largely contributed by their different representations of topography over the Himalayas region, consistent with previous studies (e.g., Karki et al., 2017; Lin et al., 2018). ~~Climate~~Therefore, the relatively smooth topography used by climate models at coarser horizontal resolutions than 20 km ~~and thus with relatively smooth topography may underestimate the~~may result in the underestimation of aerosol transport from South Asia to the TP during the pre-monsoon season and ~~represent inappropriately the~~lead to the biases in distributions of aerosol radiative forcing in the atmosphere and surface snow over the TP.

5. Discussion

Previous studies also found the induced change of circulation and transport due to the complex topography at convection-permitting scales with the focus on the meteorological fields over the Himalayas and TP regions (e.g., Karki et al., 2017; Zhou et al., 2017, 2018; Lin et al., 2018; Wang et al., 2020). Most of them either conducted the sub-10 km simulations covering a relatively smaller region (e.g., 101×96 grids at 5 km in Karki et al., 2017; 181×121 grids at 2 km in Lin et al., 2018; ~330×230 grids at 3 km in Wang et al., 2020) compared to this study (400×300 grids at 4 km) or conducted the simulations covering the entire Himalayas

674 but at the resolutions above 10 km and with the sub-grid orographic drag parameterization to
675 consider the impact of complex topography. Although some of previous studies also showed
676 that the resolved complex topography yielded more realistic small-scale mountain-valley
677 circulations and enhanced valley winds over the Himalayas region compared to the smoother
678 topography, the overall moisture transport across the Himalayas towards the TP was weaker
679 with the complex topography due to the orographic drags.

680   The difference between previous studies and this study can be due to several factors. First,
681 previous studies focused on moisture instead of air pollutants. The spatial (horizontal and
682 vertical) distributions between air pollutants and moisture are different and may contribute to
683 the different impacts of topography on the overall transport flux across the Himalayas.
684 However, the analysis of the moisture from the simulations in this study shows the increase of
685 moisture transport (not shown) and hence the increase of precipitation over the TP with the
686 complex topography (Fig. S10). Second, most of previous studies focused on monsoon season
687 instead of pre-monsoon season. Therefore, the meteorological simulations for monsoon season
688 (June-July-August) at different resolutions are also conducted in this study. The results show
689 that the moisture transport and precipitation are reduced at the higher resolution with complex
690 topography and the meridional wind is overall weakened particularly over the central and
691 eastern Himalayas and TP (not shown), which is consistent with previous studies. This may
692 indicate that the different large-scale circulations between the two seasons (much stronger
693 southerly during the monsoon season) may also lead to different impacts of complex
694 topography on meridional winds and hence cross-Himalayas transport.

695   Since this study only demonstrates the potential impacts for a relatively short period, a
696 longer-term study should be conducted to examine the impacts of topography on aerosol
697 climatic effect over the TP in both pre-monsoon and monsoon seasons. In addition, the active
698 convection during the monsoon season may also play an important role on pollutant transport
699 across the Himalayas, which deserves further investigation. Furthermore, aerosol impact on
700 cloud and precipitation, particularly during the monsoon season, and thus on the latent heat in
701 the atmosphere and the associated responses may also depend on the complex topography.
702 Previous studies based on observations found that the rain frequency and intensity reached the
703 highest and the cloud thickness reached the deepest at the foothill of Himalayas and decreased
704 as the elevation increased up to the TP (e.g., Chen et al., 2017; Fu et al., 2018; Zhang et al.,
705 2018), which was explained by Fu et al. (2018) due to the blocking of the air flow by the steep
706 slope of southern Himalayas. However, the large amount of transported aerosol along the slope
707 from the foothill up to the TP may also play a role. These potential impacts of aerosols on

708 regional hydro-climate around the TP and over Asia using high-resolution model that can
709 resolve the complex topography of Himalayas and TP deserve further investigation.
710

711 **Data availability**

712   The released version of WRF-Chem can be downloaded from
713 http://www2.mmm.ucar.edu/wrf/users/download/get_source.html. The updated USTC
714 version of WRF-Chem can be downloaded from <u>http://aemol.ustc.edu.cn/product/list/</u> or
715 contact chunzhao@ustc.edu.cn. Also, the code modifications will be incorporated the release
716 version of WRF-Chem in future.
717

718 **Author contributions**

719   Meixin Zhang and Chun Zhao designed the experiments, conducted and analyzed the
720 simulations. All authors contributed to the discussion and final version of the paper.
721

722 **Acknowledgements**

730

Reference

Bansal, O., Singh, A., and Singh, D.: Characteristics of Black Carbon aerosols over Patiala Northwestern part of the IGP: Source apportionment using cluster and CWT analysis, Atmospheric Pollution Research, 10, 244–256, doi:10.1016/j.apr.2018.08.001, 2019.

Barnard, J. C., Fast, J. D., Paredes-Miranda, G., Arnott, W. P., and Laskin, A.: Technical Note: Evaluation of the WRF-Chem "Aerosol Chemical to Aerosol Optical Properties" Module using data from the MILAGRO campaign, Atmos. Chem. Phys., 10, 7325–7340, doi:10.5194/acp-10-7325-2010, 2010.

Beljaars, A. C., Brown, A. R., and Wood, N.: A new parametrization of turbulent orographic form drag, QJ Roy. Meteorol. Soc., 130, 1327-1347, doi: 10.1256/qj.03.73, 2004.

Barnett, T. P., Adam, J. C., and Lettenmaier, D. P.: Potential impacts of a warming climate on water availability in snow-dominated regions, Nature, 438, 303–309, doi:10.1038/nature04141, 2005.

Binkowski, F. S. and Shankar, U.: The Regional Particulate Matter Model: 1. Model description and preliminary results, J. Geophys. Res., 100, 26191, doi:10.1029/95JD02093, 1995.

Bookhagen, B. and Burbank, D. W.: Toward a complete Himalayan hydrological budget: Spatiotemporal distribution of snowmelt and rainfall and their impact on river discharge, J. Geophys. Res., 115, 39, doi:10.1029/2009JF001426, 2010.

Boos, W. R. and Kuang, Z.: Sensitivity of the South Asian monsoon to elevated and non-elevated heating, Scientific reports, 3, 1192, doi:10.1038/srep01192, 2013.

Cannon, F., Carvalho, L. M. V., Jones, C., Norris, J., Bookhagen, B., and Kiladis, G. N.: Effects of topographic smoothing on the simulation of winter precipitation in High Mountain Asia, J. Geophys. Res. Atmos., 122, 1456–1474, doi:10.1002/2016JD026038, 2017.

Cao, J., Tie, X., Xu, B., Zhao, Z., Zhu, C., Li, G., and Liu, S.: Measuring and modeling black carbon (BC) contamination in the SE Tibetan Plateau, Journal of Atmospheric Chemistry, 67, 45-60, doi:10.1007/s10874-011-9202-5, 2010.

Carrera, M. L., Gyakum, J. R., and Lin, C. A.: Observational Study of Wind Channeling within the St. Lawrence River Valley, J. Appl. Meteorol. Clim., 48, 2341–2361, doi:10.1175/2009JAMC2061.1, 2009.

Chapman, E. G., Gustafson, W. I., Easter, R. C., Barnard, J. C., Ghan, S. J., Pekour, M. S., and Fast, J. D.: Coupling aerosol-cloud-radiative processes in the WRF-Chem model:

767   Investigating the radiative impact of elevated point sources, Atmos. Chem. Phys., 9, 945–

768   964, doi:10.5194/acp-9-945-2009, 2009.

769   Chen, J. and Bordoni, S.: Orographic Effects of the Tibetan Plateau on the East Asian Summer

770   Monsoon: An Energetic Perspective, J. Climate, 27, 3052–3072, doi:10.1175/JCLI-D-13-

771   00479.1, 2014.

772   Chen, X., Kang, S., Cong, Z., Yang, J., and Ma, Y.: Concentration, temporal variation, and

773   sources of black carbon in the Mt. Everest region retrieved by real-time observation and

774   simulation, Atmos. Chem. Phys., 18, 12859–12875, doi:10.5194/acp-18-12859-2018, 2018.

775   Chen, Y., Fu, Y., Xian, T., and Pan, X.: Characteristics of cloud cluster over the steep southern

776   slopes of the Himalayas observed by CloudSat, Int. J. Climatol., 37, 4043–4052,

777   doi:10.1002/joc.4992, 2017.

778   Cong, Z., Kang, S., and Qin, D.: Seasonal features of aerosol particles recorded in snow from

779   Mt. Qomolangma (Everest) and their environmental implications, Journal of environmental

780   sciences (China), 21, 914–919, doi:10.1016/S1001-0742(08)62361-X, 2009.

781   Cong, Z., Kang, S., Kawamura, K., Liu, B., Wan, X., Wang, Z., Gao, S., and Fu, P.:

782   Carbonaceous aerosols on the south edge of the Tibetan Plateau: concentrations, seasonality

783   and sources, Atmos. Chem. Phys., 15, 1573–1584, doi:10.5194/acp-15-1573-2015, 2015a.

784   Cong, Z., Kawamura, K., Kang, S., and Fu, P.: Penetration of biomass-burning emissions from

785   South Asia through the Himalayas: new insights from atmospheric organic acids, Scientific

786   reports, 5, 9580, doi:10.1038/srep09580, 2015b.

787   Dentener, F., Kinne, S., Bond, T., Boucher, O., Cofala, J., Generoso, S., Ginoux, P., Gong, S.,

788   Hoelzemann, J. J., Ito, A., Marelli, L., Penner, J. E., Putaud, J. P., Textor, C., Schulz, M.,

789   van der Werf, G. R., and Wilson, J.: Emissions of primary aerosol and precursor gases in the

790   years 2000 and 1750, prescribed data-sets for AeroCom, Atmos. Chem. Phys., 6, 4321–4344,

791   doi:10.5194/acp-6-4321-2006, 2006.

792   Ding, Y., Sun, Y., Wang, Z., Zhu, Y., and Song, Y.: Inter-decadal variation of the summer

793   precipitation in China and its association with decreasing Asian summer monsoon Part II:

794   Possible causes, Int. J. Climatol., 29, 1926–1944, doi:10.1002/joc.1759, 2009.

795   Du, Q., Zhao, C., Zhang, M., Dong, X., Chen, Y., Liu, Z., Hu, Z., Zhang, Q., Li, Y., Yuan, R.

796   , and Miao, S.: Modelling diurnal variation of surface PM2.5 concentration over East China

797   with WRF-Chem: Impacts from boundary layer mixing and anthropogenic

798   emission, Atmos. Chem. Phys., 20, 2839–2863, doi:10.5194/acp-20-2839-2020, 2020.

799 Duan, A. M. and Wu, G. X.: Role of the Tibetan Plateau thermal forcing in the summer climate

800   patterns over subtropical Asia, Climate Dynamics, 24, 793–807, doi:10.1007/s00382-004-

801   0488-8, 2005.

802 Dubovik, O. and King, M. D.: A flexible inversion algorithm for retrieval of aerosol optical

803   properties from Sun and sky radiance measurements, J. Geophys. Res., 105, 20673–20696,

804   doi:10.1029/2000JD900282, 2000.

805 Dubovik, O., Holben, B., Eck, T. F., Smirnov, A., Kaufman, Y. J., King, M. D., Tanré, D., and

806   Slutsker, I.: Variability of Absorption and Optical Properties of Key Aerosol Types

807   Observed in Worldwide Locations, J. Atmos. Sci., 59, 590–608, doi:10.1175/1520-

808   0469(2002)059<0590:VOAAOP>2.0.CO;2, 2002.

809 Dumka, U. C., Moorthy, K. K., Kumar, R., Hegde, P., Sagar, R., Pant, P., Singh, N., and Babu,

810   S. S.: Characteristics of aerosol black carbon mass concentration over a high altitude location

811   in the Central Himalayas from multi-year measurements, Atmospheric Research, 96, 510–

812   521, doi:10.1016/j.atmosres.2009.12.010, 2010.

813 Easter, R. C., Ghan, S. J., Zhang, Y., Saylor, R. D., Chapman, E. G., Laulainen, N. S., Abdul-

814   Razzak, H., Leung, L. R., Bian, X., and Zaveri, R. A.: MIRAGE: Model Description and

815   Evaluation of Aerosols and Trace Gases, J. Geophys. Res., 109, D20210,

816   doi:10.1029/2004JD004571, 2004.

817 Egger, J., Bajracharya, S., Egger, U., Heinrich, R., Reuder, J., Shakya, P., Wendt, H., and Wirth,

818   V.: Diurnal winds in the Himalayan Kali Gandaki Valley. Part I: Observations, Mon.

819   Weather Rev., 128, 1106–1122, 2000.

820 Engling, G. and Gelencser, A.: Atmospheric Brown Clouds: From Local Air Pollution to

821   Climate Change, Elements, 6, 223–228, doi:10.2113/gselements.6.4.223, 2010.

822 Fan, J., Rosenfeld, D., Yang, Y., Zhao, C., Leung, L. R., and Li, Z.: Substantial contribution

823   of anthropogenic air pollution to catastrophic floods in Southwest China, Geophys. Res. Lett.,

824   42, 6066–6075, doi:10.1002/2015GL064479, 2015.

825 Fast, J. D., Gustafson Jr, W. I., Easter, R. C., Zaveri, R. A., Barnard, J. C., Chapman, E. G.,

826   Grell, G. A., and Peckham, S. E.: Evolution of ozone, particulates, and aerosol direct

827   radiative forcing in the vicinity of Houston using a fully coupled meteorology-chemistry-

828   aerosol model, J. Geophys. Res., 111, D21305, doi:10.1029/2005JD006721, 2006.

829 Feng, Y., Kotamarthi, V. R., Coulter, R., Zhao, C., and Cadeddu, M.: Radiative and

830   thermodynamic responses to aerosol extinction profiles during the pre-monsoon month over

831   South Asia, Atmos. Chem. Phys., 16, 247–264, doi:10.5194/acp-16-247-2016, 2016.

Flanner, M. G. and Zender, C. S.: Snowpack radiative heating: Influence on Tibetan Plateau climate, Geophys. Res. Lett., 32, L06501, doi:10.1029/2004GL022076, 2005.

Fu, Y., Pan, X., Xian, T., Liu, G., Zhong, L., Liu, Q., Li, R., Wang, Y., and Ma, M.: Precipitation characteristics over the steep slope of the Himalayas in rainy season observed by TRMM PR and VIRS, Climate dynamics, 51, 1971-1989, doi: 10.1007/s00382-017-3992-3, 2018.

Gao, Y., Zhao, C., Liu, X., Zhang, M., and Leung, L. R.: WRF-Chem simulations of aerosols and anthropogenic aerosol radiative forcing in East Asia, Atmospheric Environment, 92, 250–266, doi:10.1016/j.atmosenv.2014.04.038, 2014.

Ginoux, P., Chin, M., Tegen, I., Prospero, J. M., Holben, B., Dubovik, O., and Lin, S.-J.: Sources and distributions of dust aerosols simulated with the GOCART model, J. Geophys. Res., 106, 20255–20273, doi:10.1029/2000JD000053, 2001.

Gong, P., Wang, X., Pokhrel, B., Wang, H., Liu, X., Liu, X., and Wania, F.: Trans-Himalayan Transport of Organochlorine Compounds: Three-Year Observations and Model-Based Flux Estimation, Environ. Sci. Technol., 53, 6773–6783, doi:10.1021/acs.est.9b01223, 2019.

Gong, S. L.: A parameterization of sea-salt aerosol source function for sub- and super-micron particles, Global Biogeochem. Cycles, 17, n/a-n/a, doi:10.1029/2003GB002079, 2003.

Grell, G. A., Peckham, S. E., Schmitz, R., McKeen, S. A., Frost, G., Skamarock, W. C., and Eder, B.: Fully coupled "online" chemistry within the WRF model, Atmospheric Environment, 39, 6957–6975, doi:10.1016/j.atmosenv.2005.04.027, 2005.

Gustafson, W. I., E. G. Chapman, S. J. Ghan, R. C. Easter, and J. D. Fast: Impact on modeled cloud characteristics due to simplified treatment of uniform cloud condensation nuclei during NEAQS 2004, Geophys. Res. Lett., 34, L19809, doi:10.1029/2007GL030021, 2007.

Hansen, J. and Nazarenko, L.: Soot climate forcing via snow and ice albedos, Proceedings of the National Academy of Sciences, 101, 423–428, doi:10.1073/pnas.2237157100, 2004.

He, C., Flanner, M. G., Chen, F., Barlage, M., Liou, K. N., Kang, S., Ming, J., and Qian, Y.: Black carbon-induced snow albedo reduction over the Tibetan Plateau: uncertainties from snow grain shape and aerosol–snow mixing state based on an updated SNICAR model, Atmos. Chem. Phys., 18, 11507–11527, doi: 10.5194/acp-18-11507-2018, 2018.

He, C., Li, Q., Liou, K. N., Takano, Y., Gu, Y., Qi, L., Mao, Y., and Leung, L. R.: Black carbon radiative forcing over the Tibetan Plateau, Geophys. Res. Lett., 41, 7806–7813, doi:10.1002/2014GL062191, 2014.

He, C., Wang, Z., Zhou, T., and Li, T.: Enhanced Latent Heating over the Tibetan Plateau as a Key to the Enhanced East Asian Summer Monsoon Circulation under a Warming Climate, J. Climate, 32, 3373–3388, doi:10.1175/JCLI-D-18-0427.1, 2019.

Hess, M., Koepke, P., and Schult, I.: Optical Properties of Aerosols and Clouds: The Software Package OPAC, Bull. Amer. Meteor. Soc., 79, 831–844, doi:10.1175/1520-0477(1998)079<0831:OPOAAC>2.0.CO;2, 1998.

Hindman, E. E. and Upadhyay, B. P.: Air pollution transport in the Himalayas of Nepal and Tibet during the 1995–1996 dry season, Atmospheric Environment, 36, 727–739, doi:10.1016/S1352-2310(01)00495-2, 2002.

Holben, B. N., Eck, T. F., Slutsker, I., Tanré, D., Buis, J. P., Setzer, A., Vermote, E., Reagan, J. A., Kaufman, Y. J., Nakajima, T., Lavenu, F., Jankowiak, I., and Smirnov, A.: AERONET—A Federated Instrument Network and Data Archive for Aerosol Characterization, Remote Sensing of Environment, 66, 1–16, doi:10.1016/S0034-4257(98)00031-5, 1998.

Holben, B. N., Tanre, D., Smirnov, A., ECK T. F., Slutsker, I., Abuhassan, N., Newcomb, W., Schafer, J., Chatenet, B., Lavenu, F., Kaufman, Y., Vande Castle, J., Setzer, A., Markham, B., Clark, D., Frouin, R., Halthore, R., Karneli, A., O'Neill, N., Pietras, C., Pinker, R., Voss, K., and Zibordi, G.: An emerging ground-based aerosol climatology: Aerosol optical depth from AERONET, J. Geophys. Res., 106, 12067-12097, doi:10.1029/2001JD900014, 2001.

Horvath, K., Koracin, D., Vellore, R., Jiang, J., and Belu, R.: Sub‐kilometer dynamical downscaling of near‐surface winds in complex terrain using WRF and MM5 mesoscale models, J. Geophys. Res. Atmos., 117, D11111, doi:10.1029/2012JD017432, 2012

Hu, Z., Huang, J., Zhao, C., Bi, J., Jin, Q., Qian, Y., Leung, L. R., Feng, T., Chen, S., and Ma, J.: Modeling the contributions of Northern Hemisphere dust sources to dust outflow from East Asia, Atmospheric Environment, 202, 234–243, doi:10.1016/j.atmosenv.2019.01.022, 2019.

Hu, Z., Huang, J., Zhao, C., Jin, Q., Ma, Y., and Yang, B.: Modeling dust sources, transport, and radiative effects at different altitudes over the Tibetan Plateau, Atmos. Chem. Phys. Discuss., https://doi.org/10.5194/acp-2019-431, in press, 2020.

Hu, Z., Zhao, C., Huang, J., Leung, L. R., Qian, Y., Yu, H., Huang, L., and Kalashnikova, O.V.: Trans-pacific transport and evolution of aerosols: Evaluation of quasi global WRF-Chem simulation with multiple observations, Geosci. Model Dev., 9, 1725–1746, doi:10.5194/gmd-9-1725-2016, 2016.

899 Huang, X., Song, Y., Zhao, C., Cai, X., Zhang, H., and Zhu, T.: Direct Radiative Effect by
900   Multicomponent Aerosol over China, J. Climate, 28, 3472–3495, doi:10.1175/JCLI-D-14-
901   00365.1, 2015.

902 Iacono, M. J., Mlawer, E. J., Clough, S. A., and Morcrette, J. J.: Impact of an improved
903   longwave radiation model, RRTM, on the energy budget and thermodynamic properties of
904   the NCAR community climate model, CCM3, J. Geophys. Res., 105, 14873–14890,
905   doi:10.1029/2000JD900091, 2000.

906 Immerzeel, W. W., van Beek, L. P. H., and Bierkens, M. F. P.: Climate change will affect the
907   Asian water towers, Science (New York, N.Y.), 328, 1382–1385,
908   doi:10.1126/science.1183188, 2010.

909 Jaeglé, L., Quinn, P. K., Bates, T. S., Alexander, B., and Lin, J. T.: Global distribution of sea
910   salt aerosols: new constraints from in situ and remote sensing observations, Atmos. Chem.
911   Phys., 11, 3137–3157, doi:10.5194/acp-11-3137-2011, 2011.

912 Janssens-Maenhout, G., Crippa, M., Guizzardi, D., Dentener, F., Muntean, M., Pouliot, G.,
913   Keating, T., Zhang, Q., Kurokawa, J., Wankmüller, R., van der Denier Gon, H., Kuenen, J.
914   J. P., Klimont, Z., Frost, G., Darras, S., Koffi, B., and Li, M.: HTAP_v2.2: a mosaic of
915   regional and global emission grid maps for 2008 and 2010 to study hemispheric transport of
916   air pollution, Atmos. Chem. Phys., 15, 11411–11432, doi:10.5194/acp-15-11411-2015,
917   2015.

918 Ji, Z. M.: Modeling black carbon and its potential radiative effects over the Tibetan Plateau,
919   Advances in Climate Change Research, 7, 139–144, doi:10.1016/j.accre.2016.10.002, 2016.

920 Ji, Z., Kang, S., Cong, Z., Zhang, Q., and Yao, T.: Simulation of carbonaceous aerosols over
921   the Third Pole and adjacent regions: distribution, transportation, deposition, and climatic
922   effects, Clim Dyn, 45, 2831–2846, doi:10.1007/s00382-015-2509-1, 2015.

923 Jiménez, P. A. and Dudhia, J.: Improving the representation of resolved and unresolved
924   topographic effects on surface wind in the WRF model, J. Appl. Meteorol. Clim., 51, 300-
925   316, doi:10.1175/JAMC-D-11-084.1, 2012.

926 Kain, J. S.: The Kain–Fritsch Convective Parameterization: An Update, J. Appl. Meteor., 43,
927   170–181, doi:10.1175/1520-0450(2004)043<0170:TKCPAU>2.0.CO;2, 2004.

928 Kang, S, Chen P, Li C, Liu B, Cong Z: Atmospheric Aerosol Elements over the Inland Tibetan
929   Plateau: Concentration, Seasonality, and Transport, Aerosol Air Qual. Res., 16, 789–800,
930   doi:10.4209/aaqr.2015.02.0307, 2016.

931 Kang, S., Q. Zhang, Y. Qian, Z. Ji, C. Li, Z. Cong, Y. Zhang, J. Guo, W. Du, J. Huang, Q. You,
932   A. K. Panday, M. Rupakheti, D. Chen, O. Gustafsson, M. H. Thiemens, and D. Qin: Linking

933   atmospheric pollution to cryospheric change in the Third Pole region: current progress and

934   future prospects, National Science Review, 6, 796–809, doi:10.1093/nsr/nwz031, 2019.

935 Kant, Y., Shaik, D. S., Mitra, D., Chandola, H. C., Babu, S. S., and Chauhan, P.: Black carbon

936   aerosol quantification over north-west Himalayas: Seasonal heterogeneity, source

937   apportionment and radiative forcing, Environmental pollution (Barking, Essex 1987),

938   113446, doi:10.1016/j.envpol.2019.113446, 2019.

939 Karki, R., ul Hasson, S., Gerlitz, L., Schickhoff, U., Scholten, T., and Böhner, J.: Quantifying

940   the added value of convection-permitting climate simulations in complex terrain: a

941   systematic evaluation of WRF over the Himalayas, Earth Syst. Dynam., 8, 507–528,

942   doi:10.5194/esd-8-507-2017, 2017.

943 Kok, J. F.: A scaling theory for the size distribution of emitted dust aerosols suggests climate

944   models underestimate the size of the global dust cycle, Proceedings of the National Academy

945   of Sciences of the United States of America, 108, 1016–1021, doi:10.1073/pnas.1014798108,

946   2011.

947 Kopacz, M., Mauzerall, D. L., Wang, J., Leibensperger, E. M., Henze, D. K., and Singh, K.:

948   Origin and radiative forcing of black carbon transported to the Himalayas and Tibetan

949   Plateau, Atmos. Chem. Phys., 11, 2837–2852, doi:10.5194/acp-11-2837-2011, 2011.

950 Kuhlmann, J. and Quaas, J.: How can aerosols affect the Asian summer monsoon? Assessment

951   during three consecutive pre-monsoon seasons from CALIPSO satellite data, Atmos. Chem.

952   Phys., 10, 4673–4688, doi:10.5194/acp-10-4673-2010, 2010.

953 Lau, K. M. and Kim, K. M.: Observational relationships between aerosol and Asian monsoon

954   rainfall, and circulation, Geophys. Res. Lett., 33, D22101, doi: 10.1029/2006GL027546,

955   2006b.

956 Lau, K. M., Kim, M. K., and Kim, K. M.: Asian summer monsoon anomalies induced by

957   aerosol direct forcing: the role of the Tibetan Plateau, Clim Dyn, 26, 855–864, doi:

958   10.1007/s00382-006-0114-z, 2006a.

959 Lau, W. K. and Kim, K. M.: Impact of Snow Darkening by Deposition of Light-Absorbing

960   Aerosols on Snow Cover in the Himalayas–Tibetan Plateau and Influence on the Asian

961   Summer Monsoon: A Possible Mechanism for the Blanford Hypothesis, Atmosphere, 9, 438,

962   doi:10.3390/atmos9110438, 2018.

963 Lau, W. K. M., Kim, K. M., Shi, J. J., Matsui, T., Chin, M., Tan, Q., Peters-Lidard, C., and

964   Tao, W. K.: Impacts of aerosol–monsoon interaction on rainfall and circulation over

965   Northern India and the Himalaya Foothills, Clim Dyn, 49, 1945–1960, doi:10.1007/s00382-

966   016-3430-y, 2017.

Lau, W. K. M., Kim, M. K., Kim, K. M., and Lee, W. S.: Enhanced surface warming and accelerated snow melt in the Himalayas and Tibetan Plateau induced by absorbing aerosols, Environ. Res. Lett., 5, 25204, doi:10.1088/1748-9326/5/2/025204, 2010.

Lee, W. S., Bhawar, R. L., Kim, M. K., and Sang, J.: Study of aerosol effect on accelerated snow melting over the Tibetan Plateau during boreal spring, Atmospheric Environment, 75, 113–122, doi:10.1016/j.atmosenv.2013.04.004, 2013.

Li, C., Bosch, C., Kang, S., Andersson, A., Chen, P., Zhang, Q., Cong, Z., Chen, B., Qin, D., and Gustafsson, Ö.: Sources of black carbon to the Himalayan–Tibetan Plateau glaciers, Nat Commun, 7, 4825, doi:10.1038/ncomms12574, 2016.

Li, M., Zhang, Q., Kurokawa, J. i., Woo, J. H., He, K., Lu, Z., Ohara, T., Song, Y., Streets, D. G., Carmichael, G. R., Cheng, Y., Hong, C., Huo, H., Jiang, X., Kang, S., Liu, F., Su, H., and Zheng, B.: MIX: a mosaic Asian anthropogenic emission inventory under the international collaboration framework of the MICS-Asia and HTAP, Atmos. Chem. Phys., 17, 935–963, doi:10.5194/acp-17-935-2017, 2017.

Li, R. and Min, Q. L.: Impacts of mineral dust on the vertical structure of precipitation, J. Geophys. Res., 115, 1337, doi:10.1029/2009JD011925, 2010.

Li, R., Dong, X., Guo, J., Fu, Y., Zhao, C., Wang, Y., and Min, Q.: The implications of dust ice nuclei effect on cloud top temperature in a complex mesoscale convective system, Sci Rep, 7, 291, doi:10.1038/s41598-017-12681-0, 2017.

Li, R., Shao, W., Guo, J., Fu, Y., Wang, Y., Liu, G., Zhou, R., and Li, W.: A Simplified Algorithm to Estimate Latent Heating Rate Using Vertical Rainfall Profiles Over the Tibetan Plateau, J. Geophys. Res. Atmos., 124, 942–963, doi:10.1029/2018JD029297, 2019.

Lin, C., Chen, D., Yang, K., and Ou, T.: Impact of model resolution on simulating the water vapor transport through the central Himalayas: implication for models' wet bias over the Tibetan Plateau, Clim Dyn, 51, 3195–3207, doi:10.1007/s00382-018-4074-x, 2018.

Liu, P., Tsimpidi, A. P., Hu, Y., Stone, B., Russell, A. G., and Nenes, A.: Differences between downscaling with spectral and grid nudging using WRF, Atmos. Chem. Phys., 12, 3601–3610, doi:10.5194/acp-12-3601-2012, 2012.

Liu, Y., Sato, Y., Jia, R., Xie, Y., Huang, J., and Nakajima, T.: Modeling study on the transport of summer dust and anthropogenic aerosols over the Tibetan Plateau, Atmos. Chem. Phys., 15, 12581–12594, doi:10.5194/acp-15-12581-2015, 2015.

Liu, Z., Ming, Y., Zhao, C., Lau, N. C., Guo, J., Bollasina, M., and Yim, S. H. L.: Contribution of local and remote anthropogenic aerosols to a record-breaking torrential rainfall event in

Guangdong Province, China, Atmos. Chem. Phys., 20, 223–241, doi:10.5194/acp-20-223-2020, 2020.

Lu, Z., Streets, D. G., Zhang, Q., and Wang, S.: A novel back-trajectory analysis of the origin of black carbon transported to the Himalayas and Tibetan Plateau during 1996-2010, Geophys. Res. Lett., 39, n/a-n/a, doi:10.1029/2011GL049903, 2012.

Lüthi, Z. L., Škerlak, B., Kim, S. W., Lauer, A., Mues, A., Rupakheti, M., and Kang, S.: Atmospheric brown clouds reach the Tibetan Plateau by crossing the Himalayas, Atmos. Chem. Phys., 15, 6007–6021, doi:10.5194/acp-15-6007-2015, 2015.

Lutz, A. F., Immerzeel, W. W., Shrestha, A. B., and Bierkens, M. F. P.: Consistent increase in High Asia's runoff due to increasing glacier melt and precipitation, Nature Clim Change, 4, 587–592, doi:10.1038/nclimate2237, 2014.

Marinoni, A., Cristofanelli, P., Laj, P., Duchi, R., Calzolari, F., Decesari, S., Sellegri, K., Vuillermoz, E., Verza, G. P., and Villani, P.: Aerosol mass and black carbon concentrations, a two year record at NCO-P (5079 m, Southern Himalayas), Atmos. Chem. Phys., 10, 8551–8562, doi:10.5194/acp-10-8551-2010, 2010.

Menon, S., Koch, D., Beig, G., Sahu, S., Fasullo, J., and Orlikowski, D.: Black carbon aerosols and the third polar ice cap, Atmos. Chem. Phys., 10, 4559–4571, doi:10.5194/acp-10-4559-2010, 2010.

Ming, J., Xiao, C., Cachier, H., Qin, D., Qin, X., Li, Z., and Pu, J.: Black Carbon (BC) in the snow of glaciers in west China and its potential effects on albedos, Atmospheric Research, 92, 114–123, doi:10.1016/j.atmosres.2008.09.007, 2009.

Mlawer, E. J., Taubman, S. J., Brown, P. D., Iacono, M. J., and Clough, S. A.: Radiative transfer for inhomogeneous atmospheres: RRTM, a validated correlated-k model for the longwave, J. Geophys. Res., 102, 16663–16682, doi:10.1029/97JD00237, 1997.

Morrison, H., Thompson, G., and Tatarskii, V.: Impact of Cloud Microphysics on the Development of Trailing Stratiform Precipitation in a Simulated Squall Line: Comparison of One- and Two-Moment Schemes, Mon. Wea. Rev., 137, 991–1007, doi:10.1175/2008MWR2556.1, 2009.

Nakanishi, M. and Niino, H.: An Improved Mellor–Yamada Level-3 Model: Its Numerical Stability and Application to a Regional Prediction of Advection Fog, Boundary-Layer Meteorol, 119, 397–407, doi:10.1007/s10546-005-9030-8, 2006.

Oleson, K. W., Lawrence, D. M., Bonan, G. B., Flanner, M. G., Kluzek, E., Lawrence, P. J., Levis, S., Swenson, S. C., Thornton, P. E., Dai, A., Decker, M., Dickinson, R., Feddema, J., Heald, C. L., Hoffman, F., Lamarque, J. F., Mahowald, N., Niu, G. Y., Qian, T., Randerson,

J., Running, S., Sakaguchi, K., Slater, A., Stockli, R., Wang, A., Yang, Z. L., Zeng, X., and Zeng, X.: Technical Description of version 4.0 of the Community Land Model (CLM), Tech. Rep. NCAR/TN-478+STR, National Center for Atmospheric Research, Boulder, Colorado, USA, 2010.

Prasad, A. K. and Singh, R. P.: Comparison of MISR-MODIS aerosol optical depth over the Indo-Gangetic basin during the winter and summer seasons (2000–2005), Remote Sensing of Environment, 107, 109–119, doi:10.1016/j.rse.2006.09.026, 2007.

Qian, Y., Flanner, M. G., Leung, L. R., and Wang, W.: Sensitivity studies on the impacts of Tibetan Plateau snowpack pollution on the Asian hydrological cycle and monsoon climate, Atmos. Chem. Phys., 11, 1929–1948, doi:10.5194/acp-11-1929-2011, 2011.

Qian, Y., Yasunari, T. J., Doherty, S. J., Flanner, M. G., Lau, W. K. M., Ming, J., Wang, H., Wang, M., Warren, S. G., and Zhang, R.: Light-absorbing particles in snow and ice: Measurement and modeling of climatic and hydrological impact, Adv. Atmos. Sci., 32, 64–91, doi:10.1007/s00376-014-0010-0, 2015.

Qiu, J.: China: The third pole, Nature, 454, 393–396, doi:10.1038/454393a, 2008.

Ramanathan, V. and Carmichael, G.: Global and regional climate changes due to black carbon, Nature Geosci, 1, 221–227, doi:10.1038/ngeo156, 2008.

Ramanathan, V., Ramana, M. V., Roberts, G., Kim, D., Corrigan, C., Chung, C., and Winker, D.: Warming trends in Asia amplified by brown cloud solar absorption, Nature, 448, 575–578, doi:10.1038/nature06019, 2007.

Sarangi, C., Qian, Y., Rittger, K., Bormann, K. J., Liu, Y., Wang, H., Lin, G., and Painter, T. H.: Impact of light-absorbing particles on snow albedo darkening and associated radiative forcing over high-mountain Asia: high-resolution WRF-Chem modeling and new satellite observations. Atmos. Chem. Phys., 19, 7105–7128, doi:10.5194/acp-19-7105-2019, 2019.

Seaman, N. L., Stauffer, D. R., and Lario-Gibbs, A. M.: A Multiscale Four-Dimensional Data Assimilation System Applied in the San Joaquin Valley during SARMAP. Part I: Modeling Design and Basic Performance Characteristics, J. Appl. Meteor., 34, 1739–1761, doi:10.1175/1520-0450(1995)034<1739:AMFDDA>2.0.CO;2, 1995.

Shi, X., Wang, Y., and Xu, X.: Effect of mesoscale topography over the Tibetan Plateau on summer precipitation in China: A regional model study, Geophys. Res. Lett., 35, 255, doi:10.1029/2008GL034740, 2008.

Singh, P. and Bengtsson, L.: Hydrological sensitivity of a large Himalayan basin to climate change, Hydrol. Process., 18, 2363–2385, doi:10.1002/hyp.1468, 2004.

1067 Skamarock, W. C., Klemp, J. B., Dudhia, J., Gill, D. O., Barker, D. M., Duda, M., Huang, X.
1068 Y., Wang, W., and Powers, J. G.: A Description of the Advanced Research WRF Version 3,
1069 NCAR Technical Note, NCAR/TN-468+STR, available at: http://wrf-
1070 model.org/wrfadmin/docs/arw v2.pdf, 2008.

1071 Stauffer, D. R. and Seaman, N. L.: Use of Four-Dimensional Data Assimilation in a Limited-
1072 Area Mesoscale Model. Part I: Experiments with Synoptic-Scale Data, Mon. Wea. Rev., 118,
1073 1250–1277, doi:10.1175/1520-0493(1990)118<1250:UOFDDA>2.0.CO;2, 1990.

1074 Wagner, J. S., Gohm, A., and Rotach, M. W.: The Impact of Horizontal Model Grid Resolution
1075 on the Boundary Layer Structure over an Idealized Valley, Mon. Wea. Rev., 142, 3446–
1076 3465, doi:10.1175/MWR-D-14-00002.1, 2014.

1077 Wang, X., Gong, P., Sheng, J., Joswiak, D. R., and Yao, T.: Long-range atmospheric transport
1078 of particulate Polycyclic Aromatic Hydrocarbons and the incursion of aerosols to the
1079 southeast Tibetan Plateau, Atmospheric Environment, 115, 124–131,
1080 doi:10.1016/j.atmosenv.2015.04.050, 2015.

1081 Wang, Y., Yang, K., Zhou, X., Chen, D., Lu, H., Ouyang, L., Chen, Y., Lazhu., and Wang, B.:
1082 Synergy of orographic drag parameterization and high resolution greatly reduces biases of
1083 WRF-simulated precipitation in central Himalaya, Climate Dynamics, 54, 1729–1740,
1084 doi:10.1007/s00382-019-05080-w, 2020.

1085 Wiedinmyer, C., Akagi, S. K., Yokelson, R. J., Emmons, L. K., Al-Saadi, J. A., Orlando, J. J.,
1086 and Soja, A. J.: The Fire INventory from NCAR (FINN): a high resolution global model to
1087 estimate the emissions from open burning, Geosci. Model Dev., 4, 625–641,
1088 doi:10.5194/gmd-4-625-2011, 2011.

1089 Wu, G., Liu, Y., Dong, B., Liang, X., Duan, A., Bao, Q., and Yu, J.: Revisiting Asian monsoon
1090 formation and change associated with Tibetan Plateau forcing: I. Formation, Clim Dyn, 39,
1091 1169–1181, doi:10.1007/s00382-012-1334-z, 2012a.

1092 Wu, G., Liu, Y., He, B., Bao, Q., Duan, A., and Jin, F. F.: Thermal controls on the Asian
1093 summer monsoon, Scientific reports, 2, 404, doi:10.1038/srep00404, 2012b.

1094 Wu, G., Liu, Y., Zhang, Q., Duan, A., Wang, T., Wan, R., Liu, X., Li, W., Wang, Z., and Liang,
1095 X.: The Influence of Mechanical and Thermal Forcing by the Tibetan Plateau on Asian
1096 Climate, J. Hydrometeor., 8, 770–789, doi:10.1175/JHM609.1, 2007.

1097 Wu, L., Su, H., and Jiang, J. H.: Regional simulation of aerosol impacts on precipitation during
1098 the East Asian summer monsoon, J. Geophys. Res. Atmos., 118, 6454–6467,
1099 doi:10.1002/jgrd.50527, 2013.

Wulf, H., Bookhagen, B., and Scherler, D.: Differentiating between rain, snow, and glacier contributions to river discharge in the western Himalaya using remote-sensing data and distributed hydrological modeling, Advances in Water Resources, 88, 152–169, doi:10.1016/j.advwatres.2015.12.004, 2016.

Yang, J., Kang, S., Ji, Z., and Chen, D.: Modeling the Origin of Anthropogenic Black Carbon and Its Climatic Effect Over the Tibetan Plateau and Surrounding Regions, J. Geophys. Res. Atmos., 123, 671–692, doi:10.1002/2017JD027282, 2018.

Yasunari, T. J., Bonasoni, P., Laj, P., Fujita, K., Vuillermoz, E., Marinoni, A., Cristofanelli, P., Duchi, R., Tartari, G., and Lau, K.-M.: Estimated impact of black carbon deposition during pre-monsoon season from Nepal Climate Observatory – Pyramid data and snow albedo changes over Himalayan glaciers, Atmos. Chem. Phys., 10, 6603–6615, doi:10.5194/acp-10-6603-2010, 2010.

Ye, D. Z. and Wu, G. X.: The role of the heat source of the Tibetan Plateau in the general circulation, Meteorl. Atmos. Phys., 67, 181–198, doi:10.1007/BF01277509, 1998.

Zängl, G., Egger, J., and Wirth, V.: Diurnal Winds in the Himalayan Kali Gandaki Valley. Part II: Modeling, Mon. Wea. Rev., 129, 1062–1080, doi:10.1175/1520-0493(2001)129<1062:DWITHK>2.0.CO;2, 2001.

Zaveri, R. A. and Peters, L. K.: A new lumped structure photochemical mechanism for large-scale applications, J. Geophys. Res., 104, 30387–30415, doi:10.1029/1999JD900876, 1999.

Zaveri, R. A., Easter, R. C., Fast, J. D., and Peters, L. K.: Model for Simulating Aerosol Interactions and Chemistry (MOSAIC), J. Geophys. Res., 113, 1591, doi:10.1029/2007JD008782, 2008.

Zhang, A., Fu, Y., Chen, Y., Liu, G., and Zhang, X.: Impact of the surface wind flow on precipitation characteristics over the southern Himalayas: GPM observations, Atmospheric Research, 202, 10–22, doi:10.1016/j.atmosres.2017.11.001, 2018.

Zhang, R., Wang, H., Qian, Y., Rasch, P. J., Easter, R. C., Ma, P. L., Singh, B., Huang, J., and Fu, Q.: Quantifying sources, transport, deposition, and radiative forcing of black carbon over the Himalayas and Tibetan Plateau, Atmos. Chem. Phys., 15, 6205–6223, doi:10.5194/acp-15-6205-2015, 2015.

Zhang, R., Wang, Y., He, Q., Chen, L., Zhang, Y., Qu, H., Smeltzer, C., Li, J., Alvarado, L. M. A., Vrekoussis, M., Richter, A., Wittrock, F., and Burrows, J. P.: Enhanced trans-Himalaya pollution transport to the Tibetan Plateau by cut-off low systems, Atmos. Chem. Phys., 17, 3083–3095, doi:10.5194/acp-17-3083-2017, 2017.

1133 Zhang, Y., Kang, S., Cong, Z., Schmale, J., Sprenger, M., Li, C., Yang, W., Gao, T., Sillanpää,
1134   M., Li, X., Liu, Y., Chen, P., and Zhang, X.: Light-absorbing impurities enhance glacier
1135   albedo reduction in the southeastern Tibetan plateau, J. Geophys. Res. Atmos., 122, 6915–
1136   6933, doi:10.1002/2016JD026397, 2017.

1137 Zhang, Y., Kang, S., Sprenger, M., Cong, Z., Gao, T., Li, C., Tao, S., Li, X., Zhong, X., Xu,
1138   M., Meng, W., Neupane, B., Qin, X., and Sillanpää, M.: Black carbon and mineral dust in
1139   snow cover on the Tibetan Plateau, The Cryosphere, 12, 413–431, doi:10.5194/tc-12-413-
1140   2018, 2018.

1141 Zhao, C., Chen, S., Leung, L. R., Qian, Y., Kok, J., Zaveri, R., and Huang, J.: Uncertainty in
1142   modeling dust mass balance and radiative forcing from size parameterization, Atmos. Chem.
1143   Phys., 13, 10733–10753, doi:doi:10.5194/acp-13-10733-2013, 2013b.

1144 Zhao, C., Hu, Z., Qian, Y., Leung, L. R., Huang, J., Huang, M., Jin, J., Flanner, M., Zhang, R.,
1145   Wang, H., Yan, H., Lu, Z., and Streets, D. G.: Simulating black carbon and dust and their
1146   radiative forcing in seasonal snow: a case study over North China with field campaign
1147   measurements, Atmos. Chem. Phys., 14, 11475–11491, doi:10.5194/acp-14-11475-2014,
1148   2014.

1149 Zhao, C., Huang, M., Fast, J. D., Berg, L. K., Qian, Y., Guenther, A., Gu, D., Shrivastava, M.,
1150   Liu, Y., and Walters, S.: Sensitivity of biogenic volatile organic compounds to land surface
1151   parameterizations and vegetation distributions in California, Geosci. Model Dev, 9, 1959–
1152   1976, doi:10.5194/gmd-9-1959-2016, 2016.

1153 Zhao, C., Liu, X., and Leung, L. R.: Impact of the Desert dust on the summer monsoon system
1154   over Southwestern North America, Atmos. Chem. Phys., 12, 3717–3731, doi:10.5194/acp-
1155   12-3717-2012, 2012.

1156 Zhao, C., Liu, X., Leung, L. R., and Hagos, S.: Radiative impact of mineral dust on monsoon
1157   precipitation variability over West Africa, Atmos. Chem. Phys., 11, 1879–1893,
1158   doi:10.5194/acp-11-1879-2011, 2011.

1159 Zhao, C., Liu, X., Leung, L. R., Johnson, B., McFarlane, S. A., Gustafson, W. I., Fast, J. D.,
1160   and Easter, R.: The spatial distribution of mineral dust and its shortwave radiative forcing
1161   over North Africa: modeling sensitivities to dust emissions and aerosol size treatments,
1162   Atmos. Chem. Phys., 10, 8821–8838, doi:10.5194/acp-10-8821-2010, 2010.

1163 Zhao, C., Ruby Leung, L., Easter, R., Hand, J., and Avise, J.: Characterization of speciated
1164   aerosol direct radiative forcing over California, J. Geophys. Res. Atmos., 118, 2372–2388,
1165   doi:10.1029/2012JD018364, 2013a.

1166   Zhao, P., Zhou, X., Chen, J., Liu, G., and Nan, S.: Global climate effects of summer Tibetan
1167   Plateau, Science Bulletin, 64, 1–3, doi:10.1016/j.scib.2018.11.019, 2019.

1168   Zhou, X., Beljaars, A., Wang, Y., Huang, B., Lin, C., Chen, Y., and Wu, H.: Evaluation of
1169   WRF simulations with different selections of subgrid orographic drag over the Tibetan
1170   Plateau, J. Geophys. Res. Atmos., 122, 9759–9772, doi:10.1002/ 2017JD027212, 2017.

1171   Zhou, X., Yang, K., and Wang, Y.: Implementation of a turbulent orographic form drag scheme
1172   in WRF and its application to the Tibetan Plateau, Climate dynamics, 50, 2443-2455, doi:
1173   10.1007/s00382-017-3677-y, 2018.

1174   Zhao, Z., Cao, J., Shen, Z., Xu, B., Zhu, C., Chen, L. W. A., Su, X., Liu, S., Han, Y., Wang,
1175   G., and Ho, K.: Aerosol particles at a high-altitude site on the Southeast Tibetan Plateau,
1176   China: Implications for pollution transport from South Asia, J. Geophys. Res. Atmos., 118,
1177   11,360-11,375, doi:10.1002/jgrd.50599, 2013.

1178   Zhong, S., Qian, Y., Zhao, C., Leung, R., Wang, H., Yang, B., Fan, Ji., Yan, H., Yang, X., and
1179   Liu, D.: Urbanization-induced urban heat island and aerosol effects on climate extremes in
1180   the Yangtze River Delta region of China, Atmos. Chem. Phys., 17, 5439–5457,
1181   doi:10.5194/acp-17-5439-2017, 2017.

1182
1183
1184
1185
1186
1187
1188
1189
1190
1191
1192
1193
1194
1195
1196
1197
1198
1199
1200
1201
1202
1203
1204

1205 **Table 1.** Summary of model configurations.

Description	Selection	References
Horizontal grid spacing	20 km (D1), 4 km (D2)	
Grid dimensions	250×350, 300×400	
Topography	30 arcsec (USGS)	
Vertical layers	54 (roughly 17 layers below 2 km)	
Model top pressure	50 hPa	
Nesting approach	One-way	
Aerosol scheme	MOSAIC 8 bin	Zaveri et al., 2008
Gas-phase chemistry	CBM-Z	Zaveri and Peters, 1999
Long wave Radiation	RRTMG	Iacono et al., 2000; Zhao et
Short-wave Radiation	RRTMG	al., 2011, 2013a
Cloud Microphysics	Morrison 2-moment	Morrison et al., 2009
Cumulus Cloud	Kain-Fritsch	Kain, 2004
Planetary boundary layer	MYNN level 2.5	Nakanishi and Niino, 2006
Land surface	CLM	Oleson et al., 2010
Meteorological Forcing	ERA-Interim, 0.5°×0.66°, 6 hourly	

1206

1207
1208
1209
1210
1211
1212
1213
1214
1215
1216
1217
1218
1219
1220
1221
1222
1223
1224
1225
1226
1227
1228
1229
1230
1231
1232
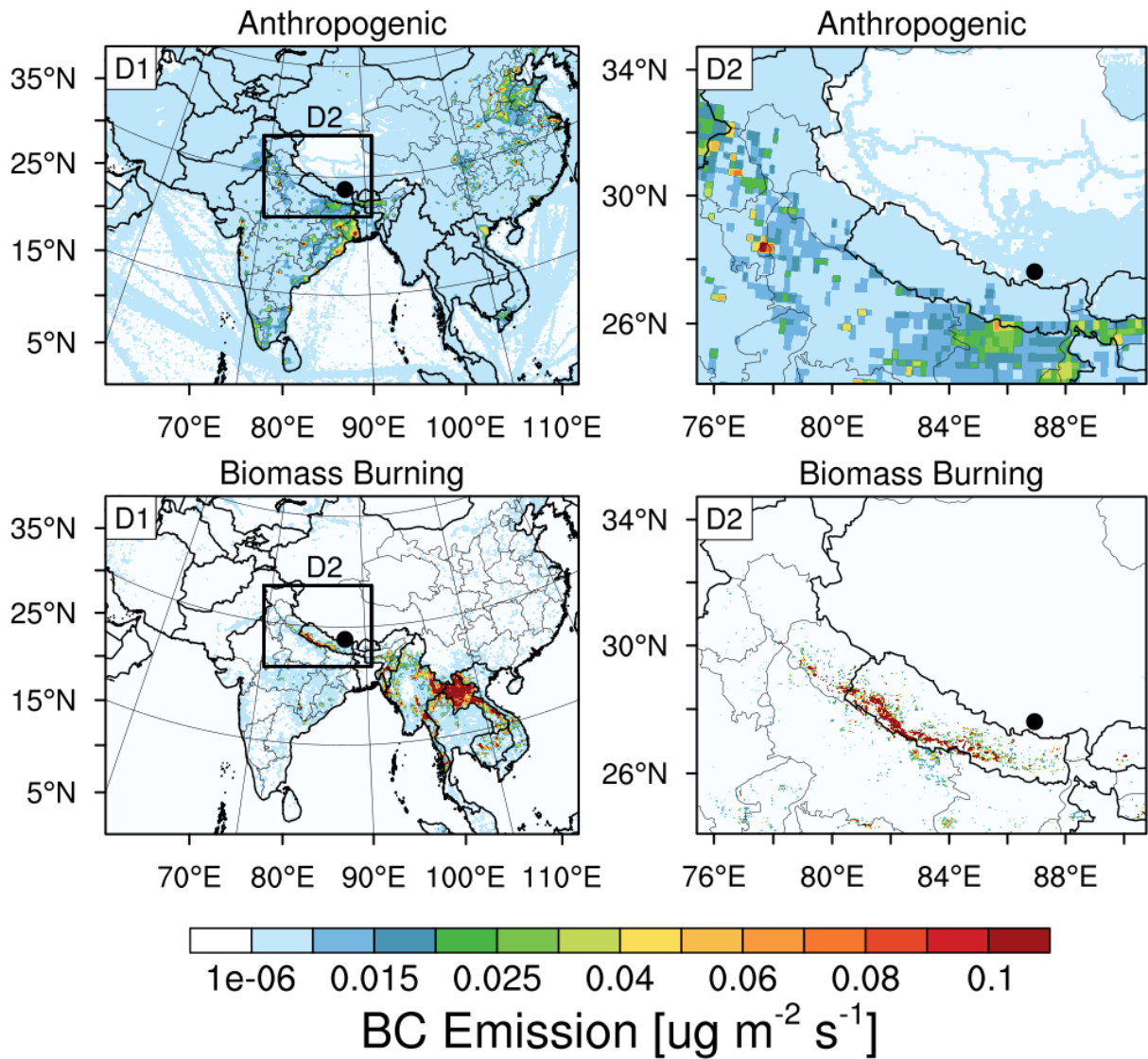
Figure 1. Anthropogenic and fire emissions over the entire simulated regions of 20-km and 4-km resolutions, the black dot represents the Qomolangma Station (QOMS, 86.95°E, 28.36°N).
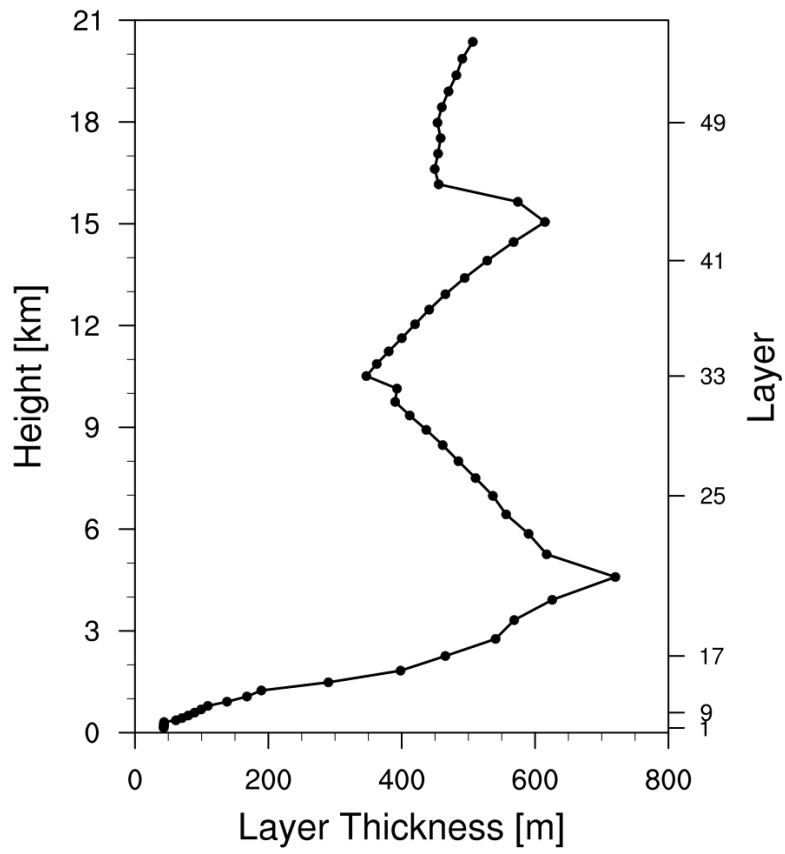
1254
Figure 2. The thickness of each vertical layer in the simulations (54 layers in total).

1256
1257
1258
1259
1260
1261
1262
1263
1264
1265
1266
1267
1268
1269
1270
1271
1272
1273
1274
1275
1276
1277
1278
1279
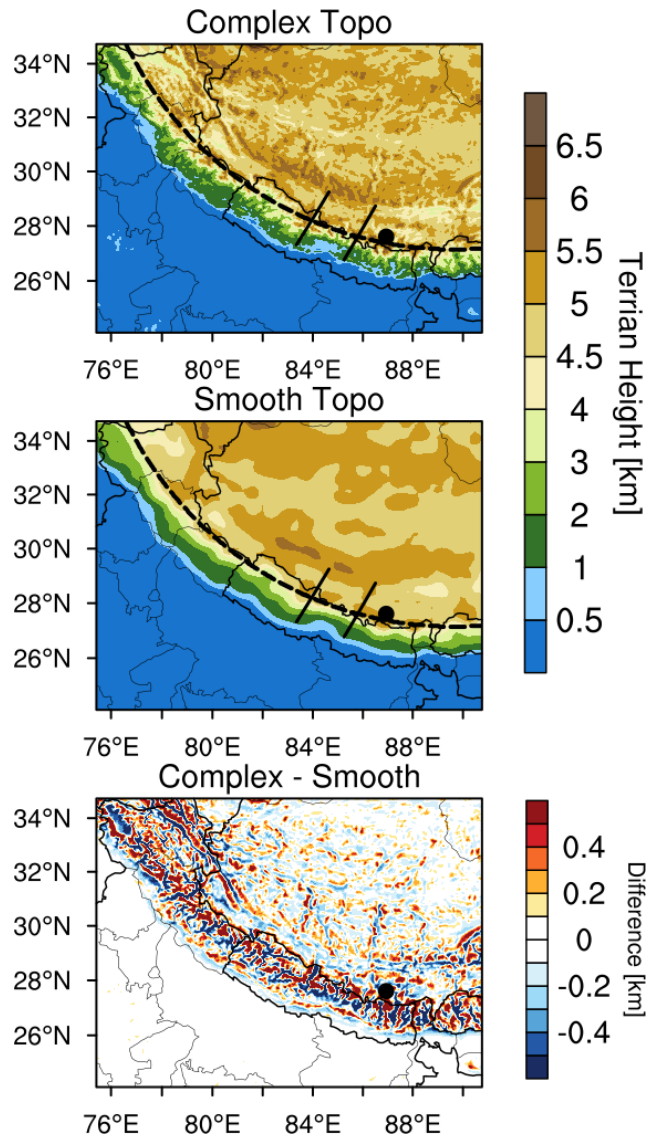
Figure 3. Spatial distributions of terrain height from the dataset at 4-km resolution (Complex Topo) and bilinearly interpolated from the 20-km resolution dataset (Smooth Topo). The one dash line and two solid lines represent the cross sections for analysis in the following.
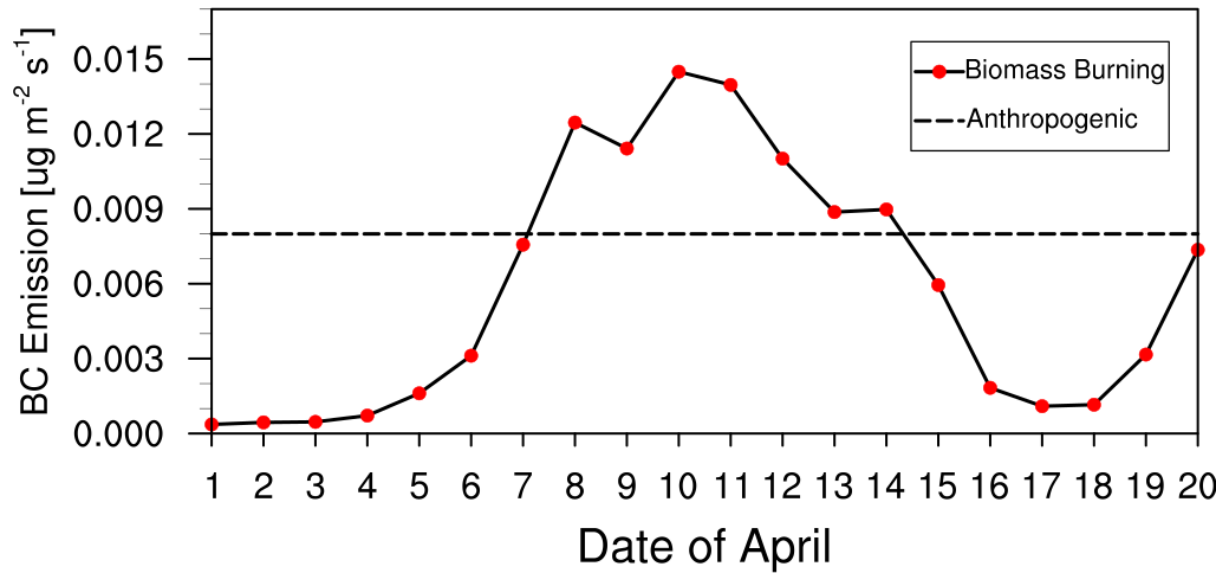
Figure 4. Time series of area-averaged daily fire emissions between 26°N and 29°N over the simulation domain at 4-km resolution (The dash line in the figure represents the anthropogenic emissions).
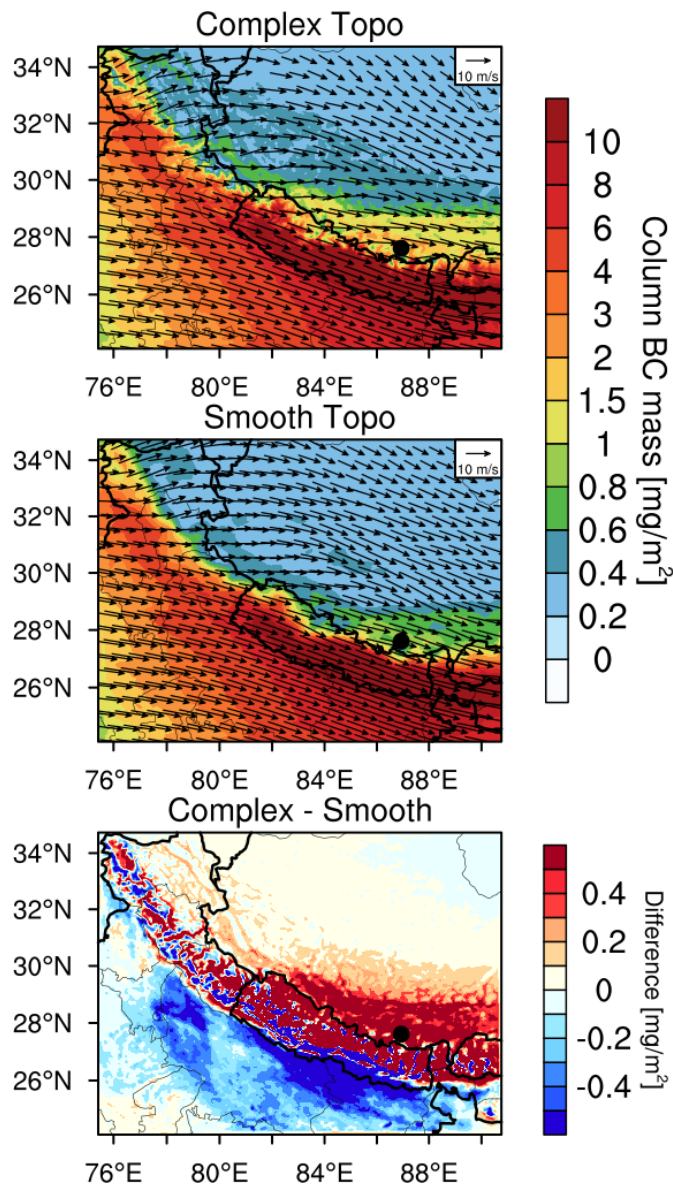
Figure 5. Spatial distributions of column integrated BC mass and the horizontal wind field at 500 hPa from the simulations with complex and smooth topography (Complex Topo and Smooth Topo) averaged for April 1-20, 2016. The difference between the two is also shown.
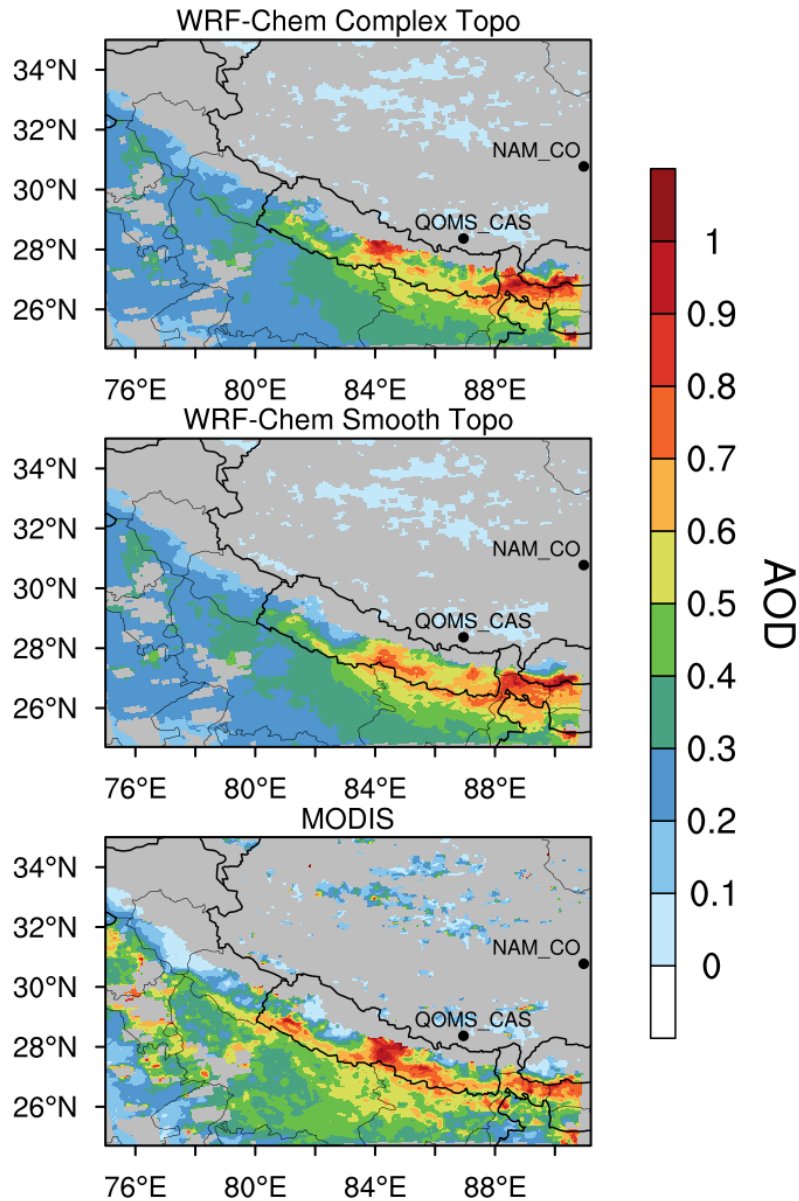
Figure 6. Spatial distributions of AOD from the MODIS retrievals and the simulations with complex and smooth topography averaged for April 1-20, 2016. The two black dots represent the two AERONET sites over the TP (QOMS_CAS, 86.95°E, 28.36°N; NAM_CO, 90.96°E, 30.77°N).
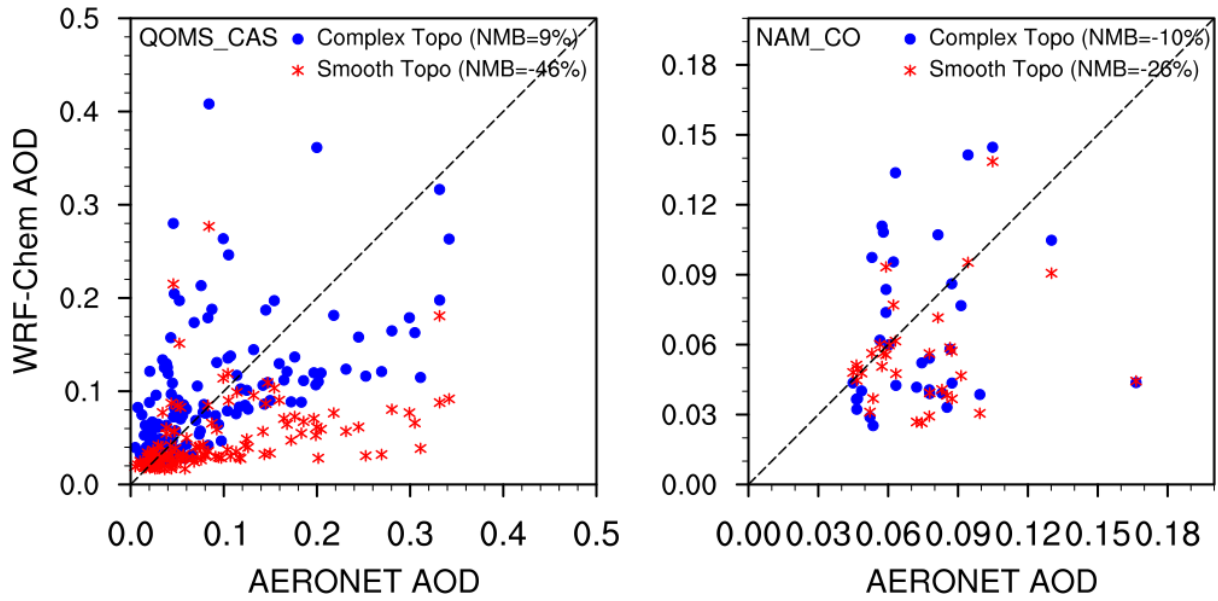
Figure 7. Hourly AOD from the measurements of AERONET and simulations by WRF-Chem at the two sites over the TP (QOMS_CAS, 86.95°E, 28.36°N; NAM_CO, 90.96°E, 30.77°N) for April 1-20, 2016.
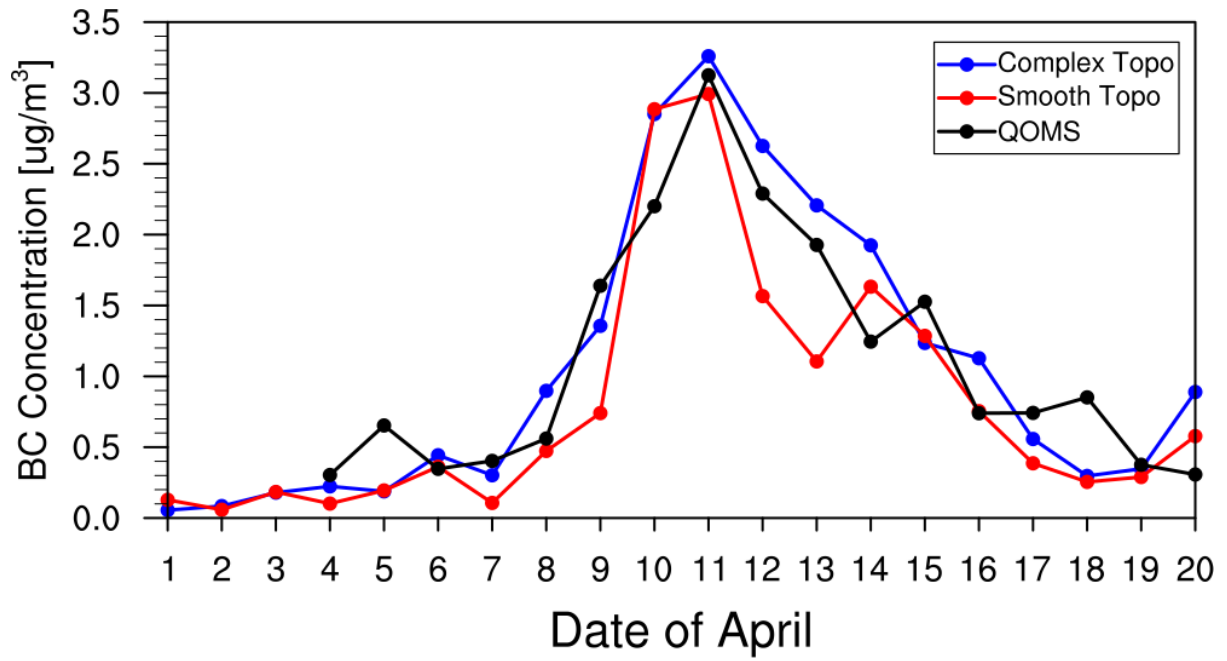
Figure 8. The simulated (colored) and observed (black) temporal variability of surface BC mass concentration at the measurement station during April 1-20 in 2016.
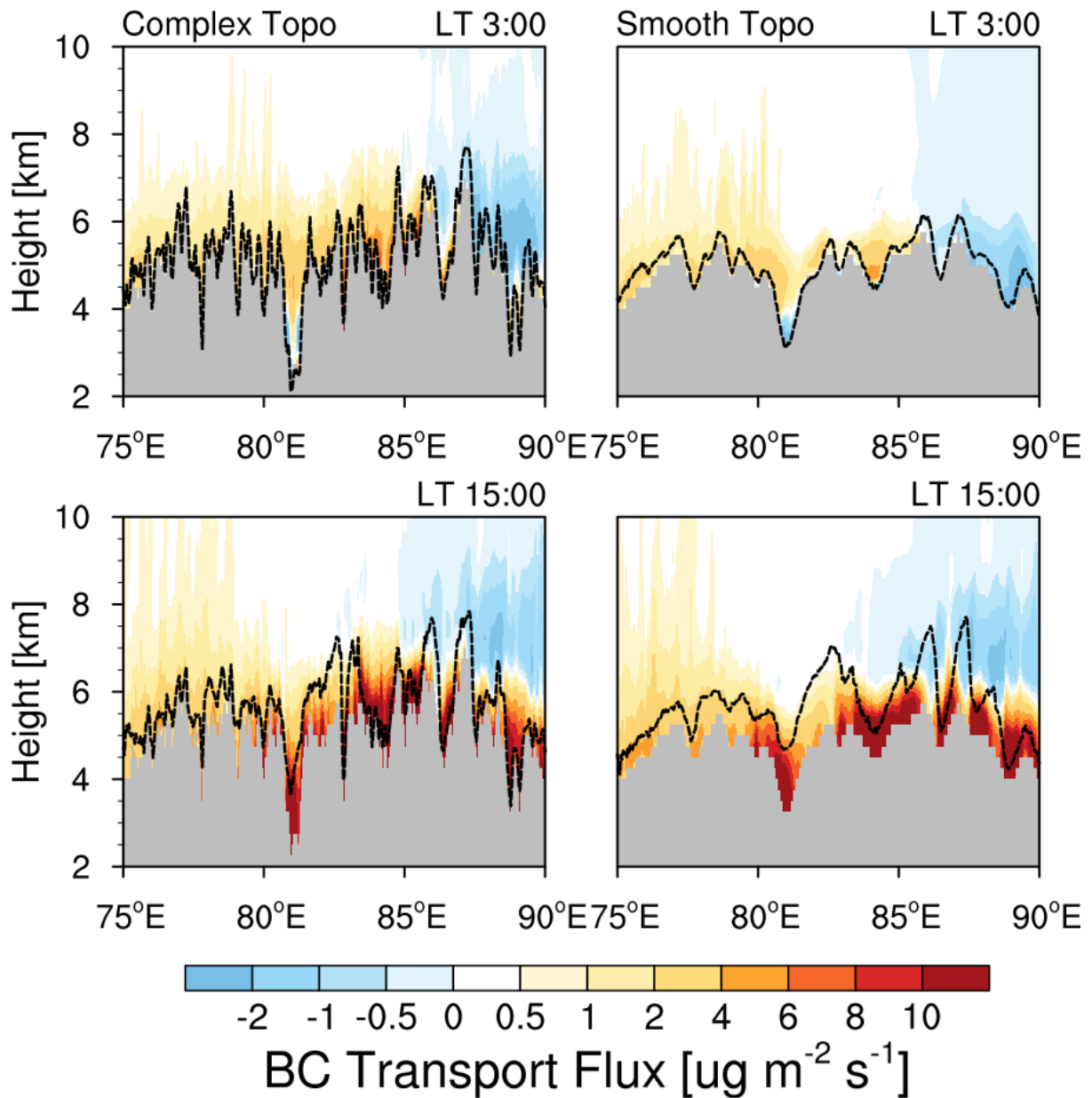
Figure 9. Longitude-height cross section of BC transport flux along the cross line (shown as the black dash line in Fig. 3) from the simulations with complex and smooth topography at local time (LT) 03:00 and 15:00 averaged for April 1-20. The PBL height along the cross section is shown here as the black dash line.
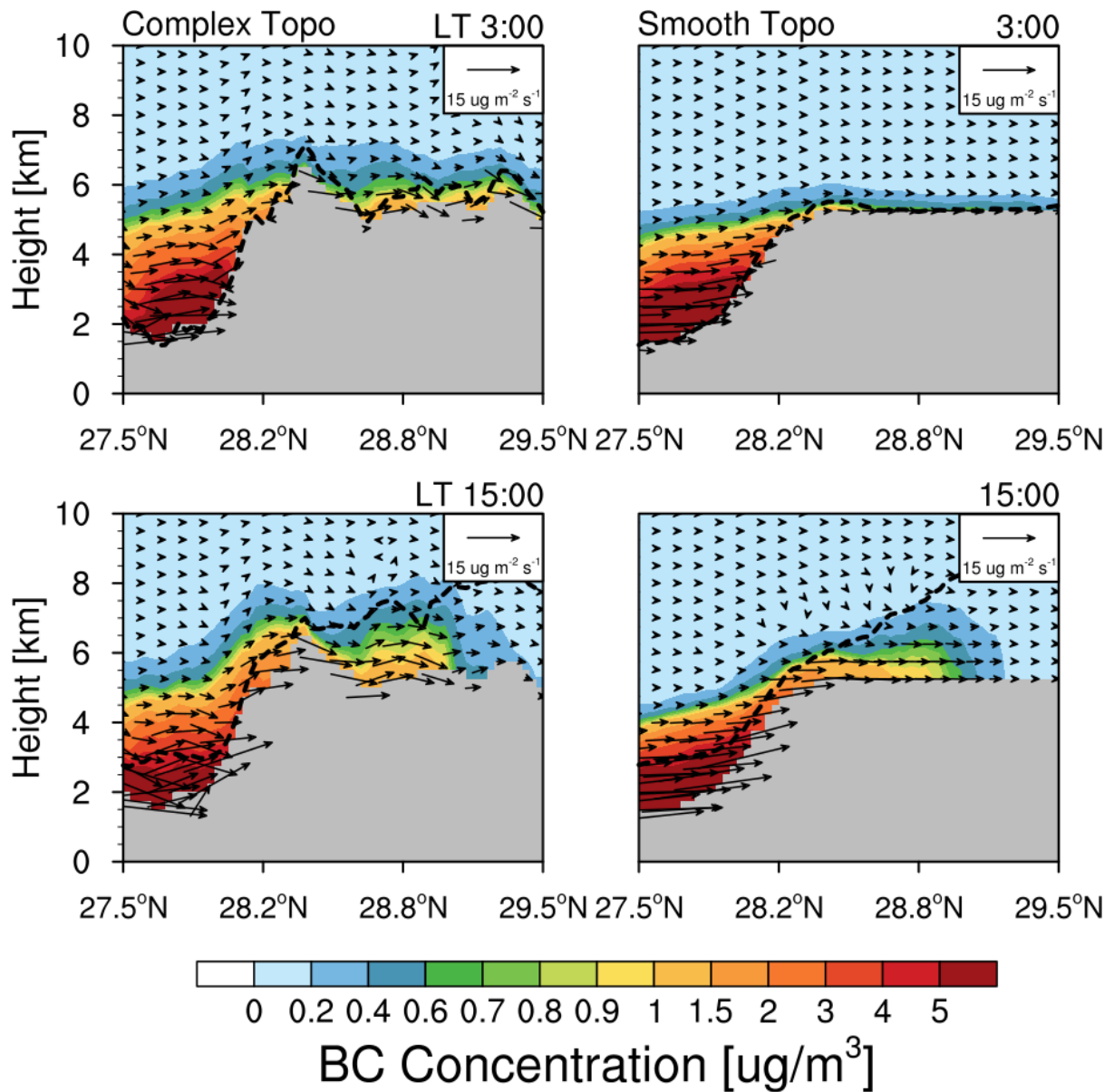
Figure 10. Latitude-height cross section of BC flux (vector) across the mountain (shown as the East black solid line in Fig.3) from the simulations with complex and smooth topography at local time (LT) 03:00 and 15:00 averaged for April 1-20, 2016. Contour represents the BC concentration.
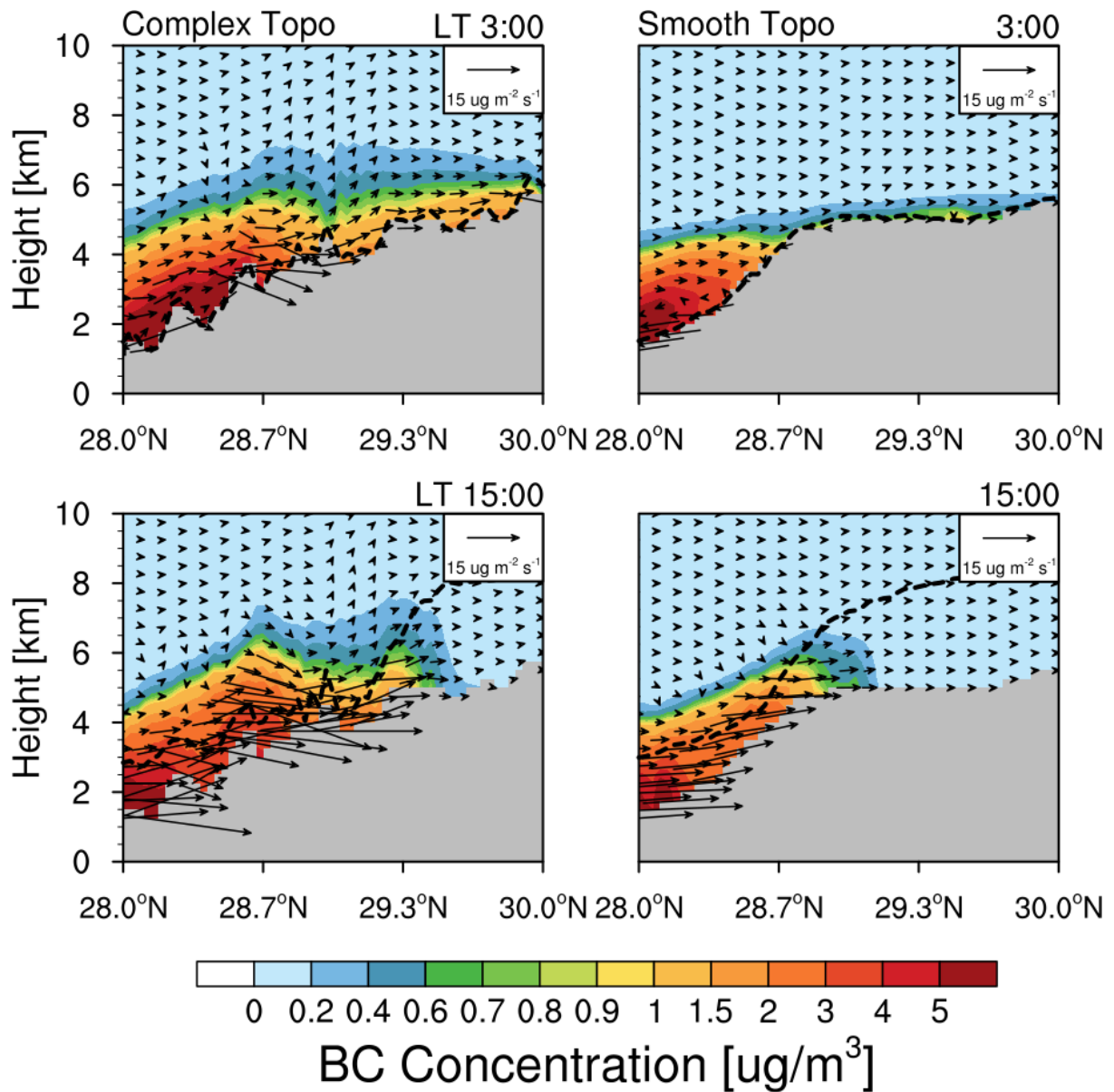
Figure 11. Latitude-height cross section of BC flux (vector) along the valley (shown as the West black solid line in Fig. 3) from the simulations with complex and smooth topography at local time (LT) 03:00 and 15:00 averaged for April 1-20, 2016. Contour represents the BC concentration.
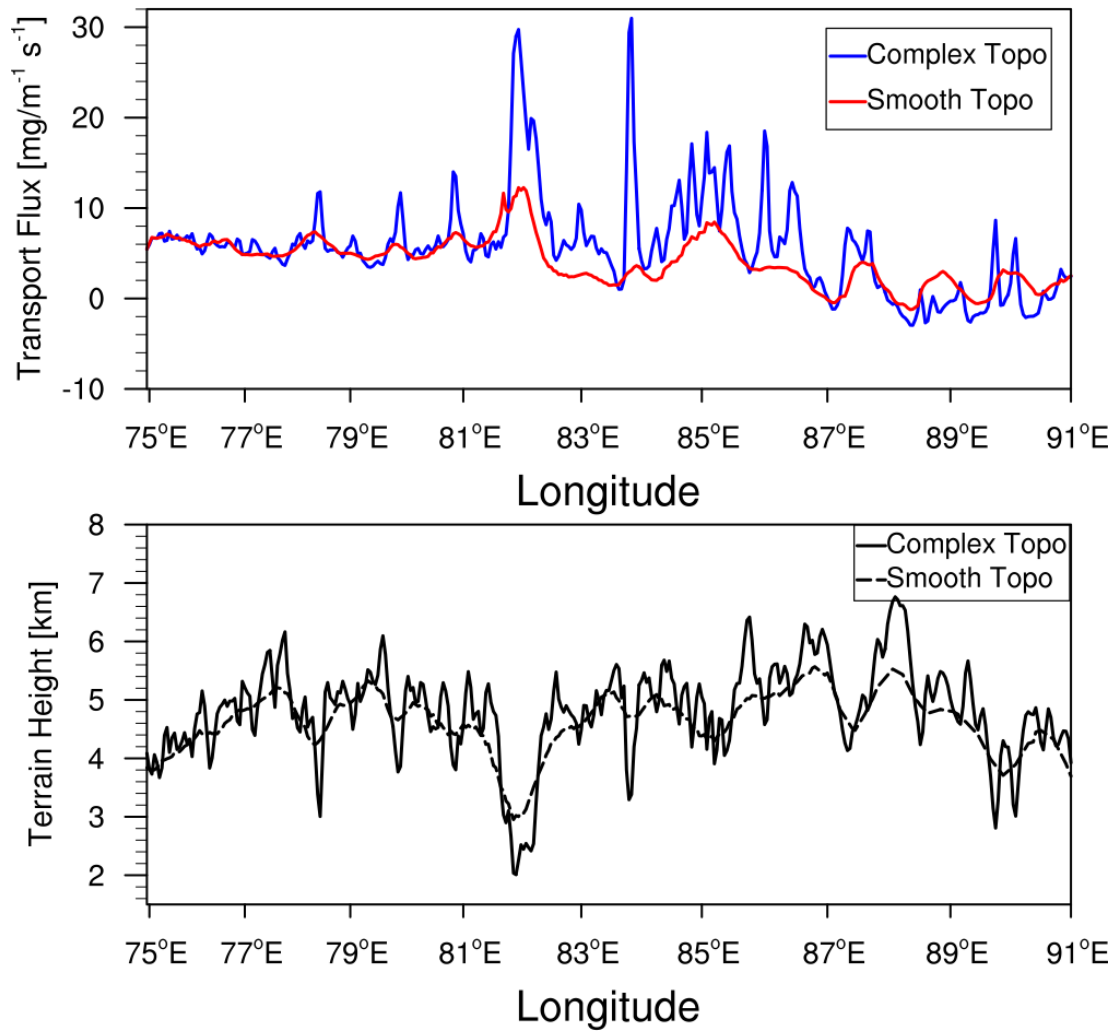
Figure 12. Longitudinal distribution of integrated BC mass flux along the cross section in Fig. 3 from the simulations with complex and smooth topography. The black lines represent the terrain heights with different topography.
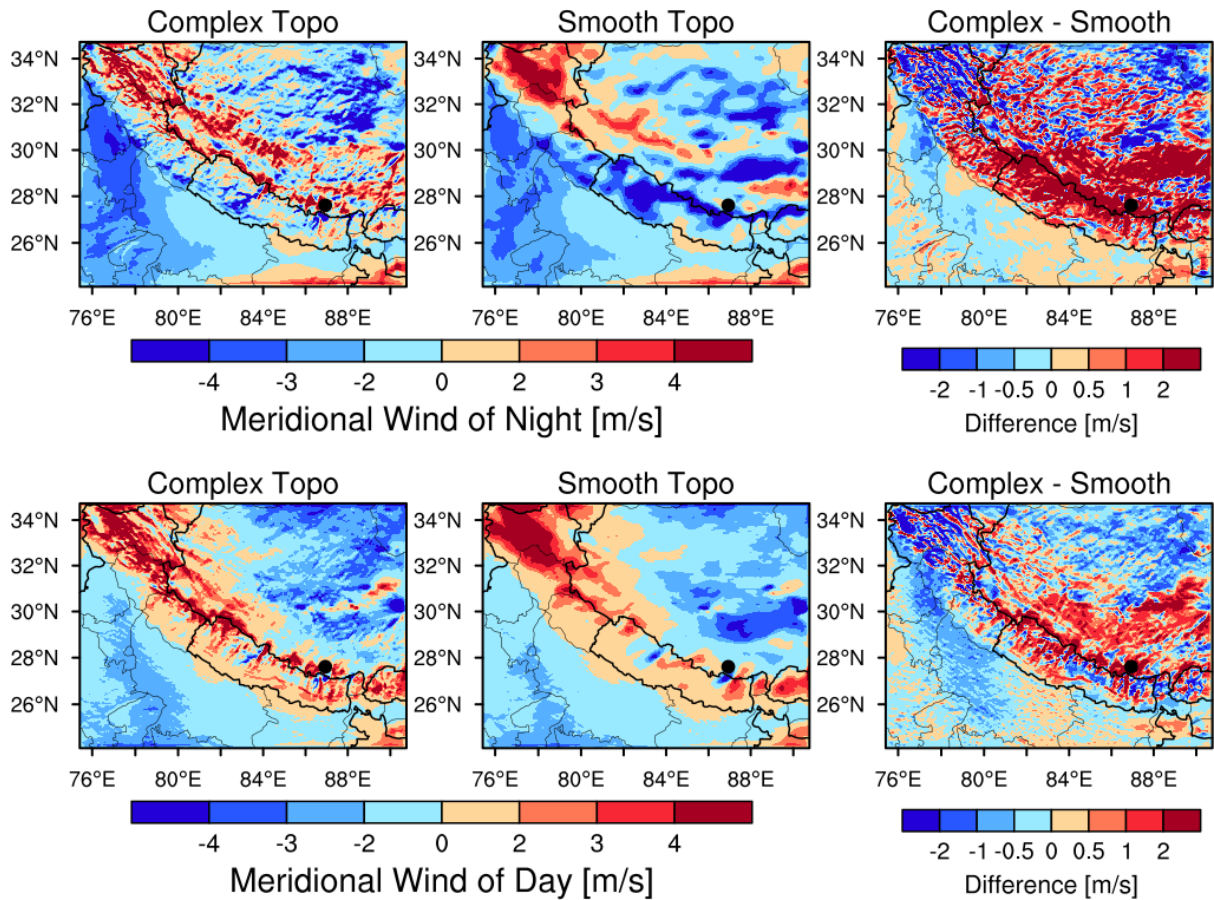
Figure 13. Spatial distributions of meridional wind speed averaged within 500 m above the ground for day and night during April 1-20, 2016 from the simulations with complex and smooth topography. The difference between the two is also shown. Nighttime is defined as local time 21:00-6:00, and daytime is defined as 9:00-18:00. Positive value denotes southerly, and negative value denotes northerly. The results averaged within 2 km above the ground are consistent.
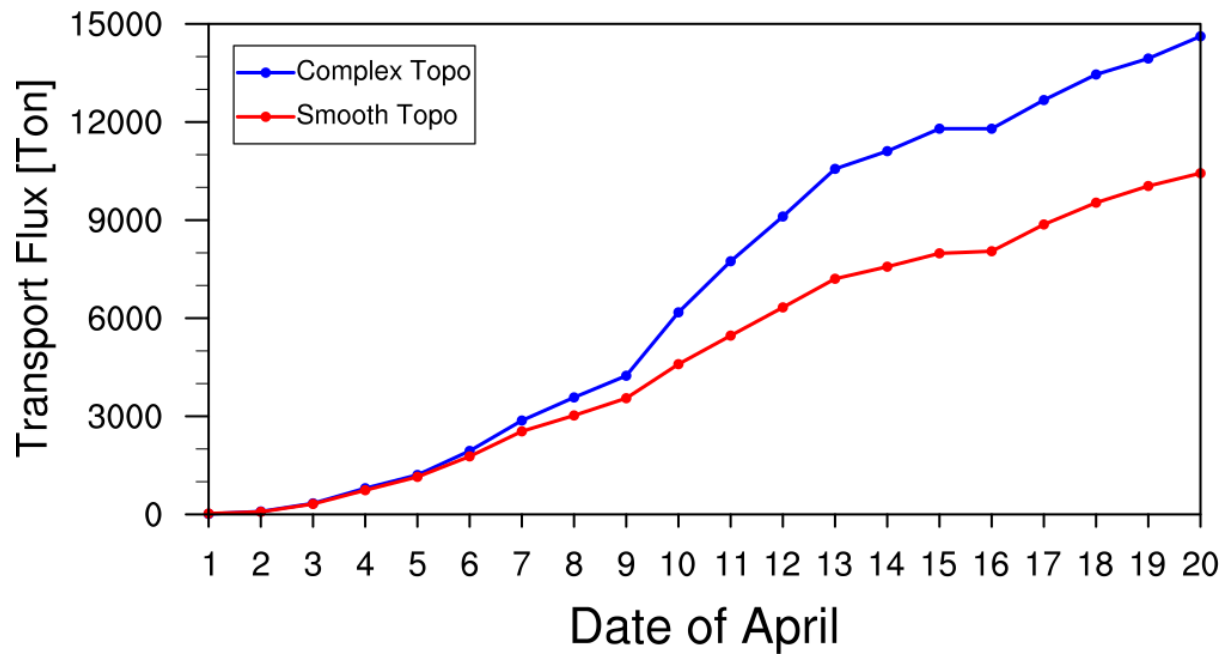
Figure 14. Accumulated integrated total transport flux of BC across the Himalayas estimated from the simulations with complex and smooth topography during April 1-20, 2016.
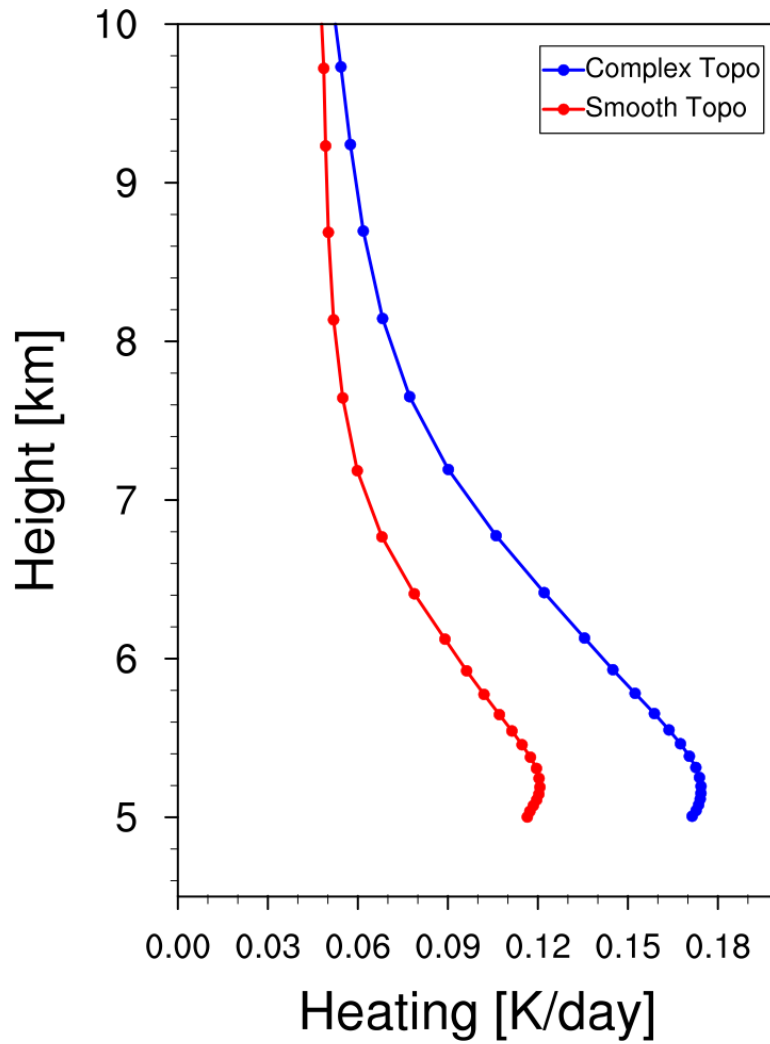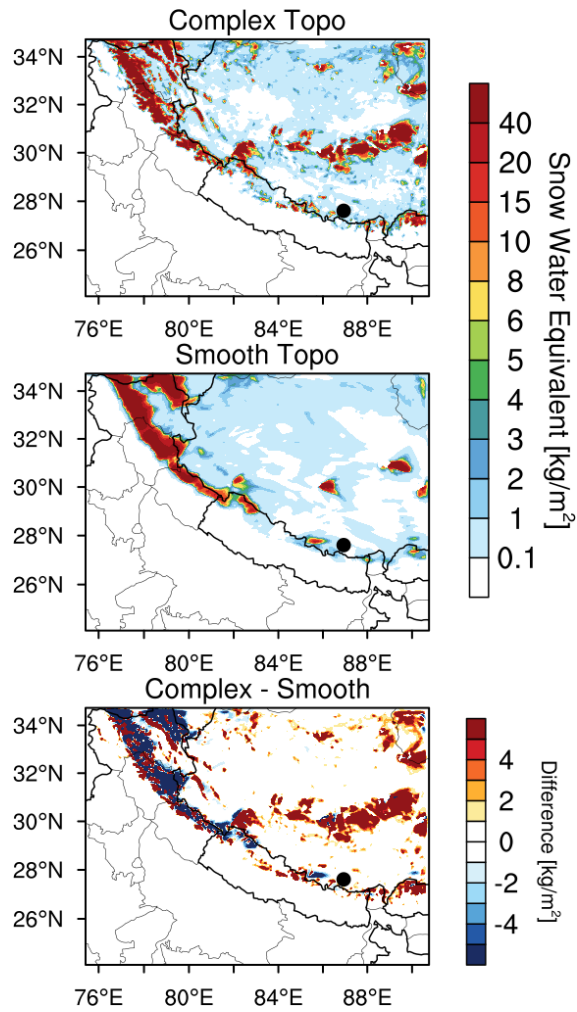
Figure 15. Vertical profiles of BC induced radiative heating rate in the atmosphere averaged over the TP (with elevation > 4 km) from the simulations with complex and smooth topography during April 1-20, 2016.

Figure 16. Spatial distributions of snow water equivalent averaged for April 1-20, 2016 from the simulations with complex and smooth topography. The difference between the two is also shown.
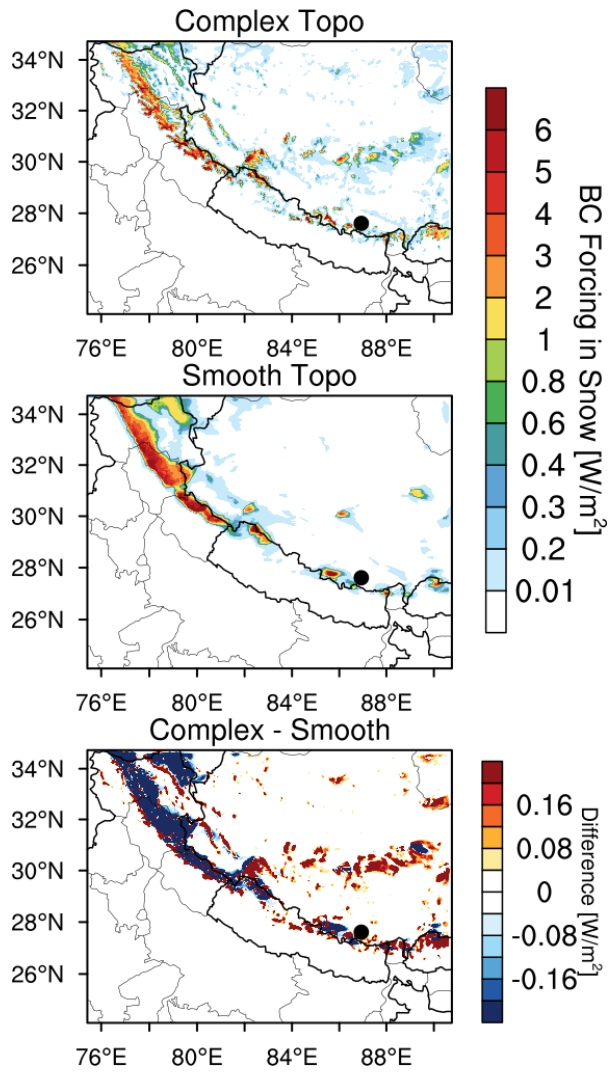
Figure 17. Spatial distributions of BC radiative forcing in the surface snow averaged for April 1-20, 2016 from the simulations with complex and smooth topography. The difference between the two is also shown.